Cosmic Magnetic Fields: Phenomenology

Krzysztof Nalewajko

31 May 2022

Contents

1 Introduction

The idea of this lecture is to provide a broad and basic overview of the cosmic magnetic fields. We wish to address the following basic questions:

- What are magnetic fields?

- Where in the Universe do we find magnetic fields?

- How do we know that magnetic fields are there?

- What is the role of magnetic fields in the Universe?

- How important are they?

Although magnetic fields do not make an important contribution to the cosmic energy density ($\Omega_B = ?$), they can be very important locally, in some cases exceeding even the rest mass energy density.

     For example, magnetic fields contribute indirectly and in various ways to the Cosmic Radiation Background (CRB) (Cooray, 2016).

1

- Main sequence stars are the main sources of the optical CRB component, and magnetic fields have important role in regulating the formation of stars.

- The radio CRB component is produced by synchrotron emission of cosmic rays propagating in magnetized interstellar medium of normal and active galaxies.

- The X-ray CRB component is produced by magnetized coronae of AGN fed by accretion disks that operate due to the magnetorotational instability (MRI) and are likely stabilized by strong toroidal magnetic fields.

- The γ-ray CRB component is produced by highly energetic particles accelerated in the relativistic jets of blazars, a class of AGN dominated by relativistically boosted non-thermal emission. The formation and acceleration of relativistic jets are driven by magnetic fields that resist the gravity of black holes and dominate other local forms of energy.

Consider the γ-ray sky as observed by the Fermi Large Area Telescope (Fermi/LAT) in the energy range $\sim (0.1-10)\,\mathrm{GeV}$ (e.g., Abdollahi et al., 2020). Besides the diffuse Galactic component produced by hadronic interactions of the cosmic rays, it contains two main classes of point sources: Galactic pulsars concentrated along the Galactic plane, and extragalactic blazars. One common characteristic of those sources is the presence of strong magnetic fields that locally dominate even the rest mass energy density of barions. Another is that they are both very efficient particle accelerators. High-energy γ-ray astronomy is one of the key drivers of astrophysical investigations of relativistically magnetized environments.

It will be shown below that a charged particle of energy $\mathcal{E}$ can be confined by magnetic field of strength B in a region of characteristic radius $R \sim \mathcal{E}/(qB)$, where q is the particle charge. This can be used to estimate the maximum energy of a particle that can be obtained in very different sources. The highest energy cosmic rays (Ultra-High-Energy Cosmic Rays, UHECR) have been measured to exceed $10^{20}\,\mathrm{eV}$. There are many potential sources of UHECR, as illustrated in the classical Hillas plot (Hillas, 1984). They range from neutron stars with $B \sim 10^{12}\,\mathrm{G}$ and $R \sim 10\,\mathrm{km}$ to the intergalactic medium (IGM) with $B \sim 10^{-9}\,\mathrm{G}$ and $R \sim 1\,\mathrm{Gpc}$. These are 21 orders of magnitude over which the same basic physical law applies.

2 Earth

Magnetism has been discovered in ancient times. Natural magnets (*lodestones*) have been mentioned by Thales of Miletus. These were pieces of the *magnetite* mineral named after the *Magnesia* region of Greece or one of its colonies in Asia Minor. The ancient Chinese knew that magnetized objects tend to orient themselves with the north-south axis. They made the early compasses in the form of 'magic spoons' that were used for certain rituals. The first written mentions of the use of compass for navigation are from the Middle Ages (Shen Kua 1088, Alexander Neckham 1190). One of the earliest known treatises on magnetism is that by Petrus Peregrinus de Maricourt (1269), who discussed the attraction and repulsion of magnetic poles, and spherical magnets (*terella*) as models of the Earth magnetic field. Further progress was made by measuring the magnetic inclination to the vertical direction (*magnetic dip*) by Robert Norman (1581). This allowed to refine the description of Earth's magnetic field in the *'De Magnete'*[1] book by William Gilbert (1600), probably the first scientific textbook on any subject.

In the XVII-th century marine navigation became a serious subject, and a lot of resources have been invested into detailed measurements of the Earth magnetic field. A compass points to the magnetic north, which differs from the geographic (true) north by magnetic declination angle, which depends on the geographic location, but has also been found to change in time (drifting to the west; Henry Gellibrand 1635). Edmond Halley attempted to explain secular changes in the Earth's magnetic field by postulating an internal structure of the Earth including a super-rotating core separated from the outer layer by fluid *effluvium* (Halley, 1683). He also produced a detailed map of magnetic declination across the Atlantic (1701).

More information about the internal structure of the Earth has been obtained from the Schiehallion experiment (1774) in which the gravitational acceleration of the Schiehallion mountain in Scotland has

---

[1]https://en.wikisource.org/wiki/On_the_Magnet

been measured[2]. What has been measured directly is a difference of $11.6''$ between vertical directions with respect to the stars at two sides of the mountain. By estimating the volume of the mountain and assuming the mean density of its rocks at 2.5 the density of water, the mean density of the Earth has been calculated as $4.5\,\mathrm{g\,cm^{-3}}$ (Hutton, 1778). This called for a dense metallic core extending over $2/3$ of the Earth radius. Earth is not hollow, but its core could be interpreted as a permanent magnet. As a bonus, this experiment allowed to estimate mean densities of other solar system bodies.

Discovery of *Curie temperature* (1895) means that a hot ($T > 1000$ K) Earth's interior cannot support permanent magnetic fields. A mechanism to continually regenerate decaying magnetic fields was necessary.

Internal structure of the Earth. Modern understanding of the internal structure of the Earth originated from the seismic studies, in particular from detections of earthquakes originating across the Earth. In 1906 Richard Oldham discovered that two types of seismic waves are detected shortly after most earthquakes: (1) primary (P) waves (arriving first) with longitudinal (compressional/pressure) perturbations that can propagate through any medium (solid or liquid), and (2) secondary (S) waves with transverse (shear) perturbations that can propagate only through solids. The arrival times of these waves are functions of the angular distance from their source. In 1912 Beno Gutenberg inferred the existence of a density discontinuity at the depth of 2900 km, identified as the *core-mantle boundary* (CMB). In 1926 Harold Jeffreys demonstrated that the core is liquid. In 1936 Inge Lehmann obtained evidence for the existence of the inner solid core.

Eventually, a modern picture of the Earth's internal structure developed, in which Earth consists of 4 main layers (for a review see Roberts & King 2013).

- *Crust*: the outermost layer, of variable depth (5-50 km), cool solid rocks with highly localized deposits of magnetized iron (magnetite) generating weak small-scale permanent magnetic fields (the magnetic curtain).

- *Mantle*: a thick layer extending to the depth of $\simeq 2900$ km, consisting of hot (up to ~ 3000 K) molten rock of density up to $\simeq 5$ g/cm^3 with very high kinematic viscosity $\nu \sim 10^{23}$ cm^2/s. Because of such high temperatures and large magnetic diffusivity ($\gtrsim 10^9$ cm^2/s), the mantle material is unmagnetized. The mantle shows a very slow large-scale convection with typical speeds of ~ 3 cm/yr ~ 1 in/yr, corresponding to the dynamical time scale of $\sim 10^8$ yr/ Such slow speeds are insufficient to maintain a dynamo in the mantle.

- *Outer core:* Below the CMB density jumps to $\simeq 10$ g/cm^3, and the material becomes dominated by metals (probably iron and nickel) with small addition of lighter elements (Si, O). The outer core, to the depth of $\simeq 5150$ km, is thought to be liquid with kinematic viscosity comparable to that of water, $\nu \sim 10^{-2}$ cm/s. The outer core is convectively unstable with typical speeds $v \sim 0.04$ cm^2/s ~ 1 in/min, corresponding to the dynamical time scale of $L/v \sim 200$ yr and the Reynolds number of $R = vL/\eta \sim 10^9$. This convection is thought to be driven by both the temperature gradient, with $\Delta T \sim 2000$ K across the outer core, and by the buoyancy of light elements extracted in the process of crystallization of the inner core. The magnetic diffusivity is estimated as $\eta \sim 7 \times 10^3$ cm^2/s, corresponding to the diffusive time scale of $\tau_\eta \sim 5 \times 10^4$ yr and the magnetic Prandtl number of $P_\mathrm{m} = \nu/\eta \sim 2 \times 10^{-6}$.

- *Inner core:* The inner core has a radius of $\simeq 1220$ km, density up to $\simeq 13$ g/cm^3, temperature at the center ~ 7000 K (hence unmagnetized). Such a high temperature is maintained by radioactive decay of various long-lived isotopes. This decay also results in a very slow decrease of the core temperature, which results in gradual crystallization of the solid core from the inside out. This process may have began somewhere in the range of $0.5 - 4$ Gyr, it leaves the inner core chemically much purer (iron/nickel) than the outer core. The inner core is estimated to be slightly elipsoidal with $\epsilon \simeq 0.0025$, and is thus tidally locked to the mantle, resulting in very little differential rotation $\lesssim 1°$/yr.

---

[2]This experiment preceded the more precise Cavendish experiment (1798).

Magnetic fields of the Earth.   Modern measurements of the Earth magnetic fields are made by ground stations and satellites. The global distribution of surface magnetic field is described by several models, e.g., the US/UK World Magnetic Model updated every 5 years[3]. In the 2020 epoch, the total magnetic field strength ranged from 0.23 G in the central part of South America extending to the east into the South Atlantic Ocean[4] to $\simeq (0.61-0.66)$ G in two locations (northern Siberia and Antractic coast sourth of Australia). This range can be compared with the equatorial surface strength of the magnetic dipole $\simeq 0.3$ G. Annual variations of the total magnetic field strength show a more complex (roughly quadrupolar) structure with values reaching $\sim \pm 0.001$ G/yr, hence up to ~ 0.1 G per century (secular variations). It is also estimated that over the past few centuries the magnetic dipole moment has been systematically decreasing at the rate of $\sim 5\%$ per century. The magnetic declination, local azimuthal angle between magnetic north and geographic north, also shows complex variations, in the case of central Europe increasing by $10'/\mathrm{yr}$, hence about $17°$ per century. It is thus drifting eastwards, opposite to the westwards drift measured in the XVII-th century. At present time, this drift is related to a rapid shift (~ 50 km/yr over the past 2 decades) of the magnetic north pole[5] (which is in fact the south magnetic pole that attracts the north poles of compass needles) across the Arctic ocean. Historically (past 400+ years) the magnetic north pole has been located over the polar islands of what is now Canada, and only since 1995 it started dashing towards the Siberia. This rapid short of the magnetic pole is interpreted as an *excursion* (temporary variation limited to higher multipole moments), rather than a *reversal* of the dipole moment. There is speculation whether a reversal of the dipole moment is imminent or already ongoing. Such an event could have severe consequences for our civilization.

The current and historic measurements of the Earth magnetic fields are supplemented by plentiful geological records. These show that there have been many reversals of the magnetic dipole moment, the most recent ones at 0.78, 2.6 and 3.6 Myr ago. These reversals are of stochastic nature, there is no preference for either of the two orientations (which strongly supports the dynamo hypothesis), there is evidence that the dipole moment has been strongly aligned with the Earth rotation axis, the intervals between the reversals follow a power-law distribution (hence it is impossible to predict when should the next reversal happen), a typical reversal may last for 1-10 kyr (which is clearly shorter than the diffusive time scale $\tau_\eta \sim 50$ kyr, indicating that reversals are sped-up by turbulent diffusion).

The angular power spectrum of the surface magnetic field (e.g., Figure 3 in Roberts & King 2013) is strongly dominated by the $l = 1$ dipole component, then shows a systematic decrease until the $l = 13$ multipole, and then becomes flat. The power of each multipole component scales like r^{-2l-4}, which allows to scale the surface power spectrum to the core-mantle boundary (CMB) using the radius ratio $r_\mathrm{s}/r_\mathrm{CMB} \simeq 1.83$. The CMB power spectrum is roughly flat for $l \leq 13$, and then systematically increasing. This indicates that only the low multipoles ($l \leq 13$) can be attributed to the core, and the high multipoles ($l > 13$) originate from the crust. The strongly inhomogeneous crust forms a *magnetic curtain* that obscures our view of the internal magnetic fields originating in the core. Nevertheless, we can map the geographic distribution of the low-order magnetic fields along the CMB and their secular variations, this shows a complex and dynamic structure, useful for constraining the dynamo models.

Such analysis is limited to the poloidal fields that have non-vanishing radial components. In addition, as has been first noted by Walter Elsasser, the core may contain strong toroidal components that would have zero flux even through the CMB. Thus, extrapolating the surface magnetic fields yields only a lower limit on the total magnetic field strength in the core. The latter parameter has been constrained indirectly to $\simeq 25$ G by modeling the Earth's nutations (short-term variations of the Earth's rotation axis) and considering the dissipation rate of tidal waves induced in the Earth outer core by gravitational forces of the Moon and Sun (Buffett, 2010).

Dynamo hypothesis.   The dynamo hypothesis, that magnetic fields within the Earth (and the Sun) are supported by electric currents, was first proposed by Joseph Larmor (1919). Its modern form has been developed by Walter Elsasser in the 1940s. In the geodynamo model, magnetic fields are generated by

---

[3]https://www.ngdc.noaa.gov/geomag/WMM/

[4]This magnetic minimum is associated with the South Atlantic Anomaly (SAA) in the cosmic-ray background, which affects many high-energy satellites including the Fermi, in case of which any data collected over the SAA are excluded from the analysis.

[5]Geophysicists distinguish the magnetic poles where local magnetic field points vertically and geomagnetic poles where magnetic dipole moment crosses the Earth.

convective circulation of the conducting liquid metals in the Earth's outer core. The convection is driven partially due to temperature gradient across the outer core (enabled by steady heat flux through the mantle and crust), and partially due to buoyancy of light elements extracted in the process of crystallization of the inner core at its boundary with the outer core. The convective cells have tubular geometry with the main axis aligned with the Earth's rotation axis (according to the Taylor-Proudman theorem), this explains the alignment of magnetic dipole with the rotation axis. The convective motions are shaped by Coriolis forces due to Earth's rotation to be helical (cyclonic), which allows generation of both toroidal field component wrapped around the tubular cells and poloidal components that extend beyond the Earth's core.

Earth's magnetosphere   The Earth's magnetic field extends into the space and forms a magnetosphere that is constantly interacting with the solar wind and strongly shaped by its pressure. The dayside magnetosphere is squeezed by the super-Alfvenic solar wind, which forms a bow shock. The interface between the solar wind and the magnetosphere is known as the dayside magnetopause, it is one of the main sites where magnetic reconnection can take place. When the mean magnetic field brought by the solar wind has a component opposite to the magnetospheric fields, reconnection may connect the solad wind fields with the Earth's magnetic poles. The nightside magnetosphere is strongly elongated, forming a magnetotail that can extend beyond the Moon's orbit. The magnetotail is another main site for magnetic reconnection, this time resulting in disconnecting the magnetospheric fields from the solar wind. Energetic particles from the solar wind can be trapped in the magnetosphere, the best example of which are the van Allen belts. As the solar wind can be strongly variable (*space weather*), reflecting dynamic variations of the solar corona, these variations can induce geomagnetic storms, the best known manifestation of which are the aurorae.

3   Planets and moons

This tour of planetary magnetic fields was inspired by their theoretical overview included in Chapter 1 of Rüdiger & Hollerbach (2004).

Moon.   The Moon shows highly irregular and weak $(3 - 1000~\mu\mathrm{G})$ surface magnetic fields, mapped in detail by the NASA Lunar Prospector mission. The Moon does not have a dynamo today, and there is no clear evidence for a dynamo in the past. There is some (anti-)correlation between magnetic field distribution and past large impacts (e.g., the strong field in the south part of the far side). Every full phase, the Moon passes through the Earth's magnetotail and its surface is impacted by magnetic fields and energetic plasma, inducing significant electric potentials $(\sim \mathrm{kV})$.

Mercury.   Mercury is a small planet impacted by the strongest solar wind, and yet it has a successful dynamo supporting a robust magnetosphere. The magnetic field of Mercury was first detected by the Mariner 10 probe (1974), and detailed measurements by the MESSENGER mission established a magnetic dipole moment of $2~\mathrm{mG} \times R_\mathrm{M}^3$ with inclination $< 3°$ and offset to the north by $0.2 R_\mathrm{M}$ (Anderson et al., 2011), where $R_\mathrm{M} = 2436~\mathrm{km}$ is the Mercury radius. Mercury has a relatively large $(\simeq 0.85 R_\mathrm{M})$ metallic core, the outer $\sim$half of which is liquid, and the inner half solid (almost the same absolute size as that of the Earth). The sidereal rotation period of Mercury is $P_\mathrm{M} = 58.6~\mathrm{d}$.

Venus.   Venus does not generate a global magnetic field, Pioneer Venus obtained an upper limit on its dipole moment $< 20~\mu\mathrm{G} \times R_\mathrm{V}^3$ (Stevenson, 1983), where $R_\mathrm{V} = 6050~\mathrm{km}$. Solar wind directly impacts the Venus atmosphere, which over time eroded it from light gases, in particular the hydrogen. Venus is extremely hot even in the crust, erasing any fossil magnetic fields in there. Lack of active plate tectonics (probably caused by the lack of water) insulates the planet interior thermally, reducing temperature gradients in the core that is found to have the size of $\simeq 0.58 R_\mathrm{V}$. The rotation period of Venus is $P_\mathrm{V} = 243~\mathrm{d}$.

Mars.   Mars also has an insignificant global field, an upper limit on the dipole moment is $< 0.1~\mathrm{mG} \times R_\mathrm{M}^3$ (Stevenson, 1983), where $R_\mathrm{M} = 3390~\mathrm{km}$. There are, however, weak localized crustal fields (probably

remnants of past global fields), but they are insufficient to shield the atmosphere from the impact of the solar wind. Mars shows seismic activity that has been studied in detail by the InSight lander. These studies indicate the presence of a liquid core of radius $0.54R_{\rm M}$ and moderate density $\simeq 6~{\rm g/cm^3}$ suggesting significant addition of light elements (Stähler et al., 2021). There is no evidence to determine the presence of an inner solid core. The lack of an active dynamo suggests than an inner core may not exist indeed. The rotation period of Mars is $P_{\rm M} = 1.026$ d.

Comparing the rocky planets.   It is an interesting case study that a smaller Mercury does have a dynamo, while a larger Mars does not. Both Venus and Mars might have had active dynamos in the past, just as they probably had water and plate tectonics, and they eventually lost all of their hydrogen. All these processes may be interrelated, and the presence of a magnetosphere is considered an important factor the habitability of planets (including the exoplanets).

Jupiter.   The magnetic field of Jupiter was discovered by means of detecting its decametric radio emission (Burke & Franklin 1955). It is the strongest field of any planet in the Solar System, with the dipole moment of $4.2 \times R_{\rm j}^3$ as determined by the Juno mission (Connerney et al. 2018), where $R_{\rm j} = 69900$ km. Jupiter is a gas giant with a thick layer of metallic hydrogen (with magnetic diffusivity of $\eta \sim 10^5~{\rm cm^2/s}$, about 10x higher than that of liquid iron) extending roughly over the radial range of $(0.3 - 0.8)R_{\rm j}$. The rotation period of Jupiter is $P_{\rm J} = 0.41$ d.

Jupiter moons.   Because of the strength of surface magnetic field, the magnetosphere of Jupiter extends to distances that encompass all of the Galilean moons. From the perspective of each moon, the relative motion of magnetic field lines induces electric fields that build up large electrostatic potentials. Additional response of the moon depends on the conductivity of its interior. The presence of a conductive layer allows to induce electric current that generate their own magnetic fields. Detection of such additional magnetic structures, in particular by the Galileo mission, has been the primary argument to postulate the presence of conductive salty oceans within Europa and Callisto.

However, the most dramatic effect of this magnetosphere is on the closest and the most peculiar moon – Io. Io is famous for its volcanic activity driven by the tremendeous tidal forces. Large electrostatic potential ionizes a significant part of the material ejected by the volcanos, turning it into a plasma the escapes Io and forms a torus of plasma orbiting Jupiter and amplifying the magnetic field strength.

Ganymede.   The largest of Jupiter moons ($R_{\rm G} = 2634$ km) has a complex internal structure including a rather small ($\sim 0.2R_{\rm G}$) iron core, the outer layer of which can be liquid. This is sufficient to sustain a dynamo that generates a global magnetic field with magnetic dipole moment of $7.2~{\rm mG} \times R_{\rm G}^3$ (Kivelson et al. 2002). This is the only such moon in the Solar System! This field is sufficiently strong to support a compact magnetosphere embeded in the much larger magnetosphere of Jupiter. The rotation period of Ganymede is $P_{\rm G} = 7.2$ d.

Saturn.   The magnetic field of Saturn is significantly weaker than that of Jupiter, with the dipole moment of $0.21~{\rm G} \times R_{\rm S}^3$ (Stevenson, 1983), where $R_{\rm S} = 58232$ km. The pressures inside Saturn are lower than in the case of Jupiter, but they still allow for the presence of a more limited layer of metallic hydrogen. The rotation period of Saturn is $P_{\rm S} = 0.44$ d.

Uranus.   The magnetic field of Uranus has only been probed during a single passage of the Voyager 2 mission in 1986. It was found to be very peculiar, with the dipole component offset by about $\simeq (1/3)R_{\rm U}$ (where $R_{\rm U} = 25360$ km) and tilted by $\simeq 59°$ from the rotation axis (itself very peculiar, almost aligned with the ecliptic) (Ness et al. 1986). The dipole moment is $\simeq 0.23~{\rm G} \times R_{\rm U}^3$, but because of the large offset the surface magnetic field strength may range from $\simeq 0.1$ G to $\simeq 1.1$ G. Uranus is already to small to support metallic hydrogen, but sufficient conductivity can be provided by methane-ammonia-water ('CNO') oceans with magnetic diffusivity of $\eta \sim 10^6~{\rm cm^2/s}$ located in relatively outer layers of the planet. The rotation period of Uranus is $P_{\rm U} = 0.72$ d.

Neptune. Our knowledge of the magnetic field of Neptune is of the same kind as that of Uranus, from the brief visit of Voyager 2 in 1989. It was found to even more peculiarly offset by $\simeq 0.55 R_N$ (where $R_N = 24620$ km) and tilted by $\simeq 47°$ (Ness et al. 1989). The dipole moment is $\simeq 0.13$ G $\times R_N^3$, and the quadrupole moment may be comparably strong. Like Uranus, Neptune is thought to operate a dynamo in outer CNO oceans. The rotation period of Neptune is $P_N = 0.67$ d.

Note that since both Uranus and Neptune are found to have peculiarly offset and tilted dipole components, this cannot be a coincidence (e.g., an ongoing field reversal). However, both the tilt and offset can be explained by localized dynamo opperating in relatively shallow subsurface layers with convectively stable interiors. The regular dipole fields generated by other planets are consistent with relatively deeper location of their convective layers.

4 Sun

Our closest star, the Sun, has long been revered as a perfect shining body, despite occasional observations of mysterious dark spots, the *sunspots*. Observations of sunspots have been recorded by the Ancient Chinese (the Book of Changes, ~800 BC), by the Ancient Greeks (Theophrastus, ≃300 BC), by Medieval Europeans (John of Worcester, 1128). More detailed observations began right after the invention of a telescope (Harriot, Fabricius, Scheiner, Galileo, ≃1610).

Sunspots reveal that the Sun is rotating, but not like a rigid body. The sidereal rotation period is the shortest along the equator ($\simeq 25$ d) and the longest at the poles ($\simeq 34$ d). Evidence for *differential rotation* extends deep into the Sun's interior, across the entire *convective zone* ($r > 0.7 R_\odot$), as probed by the helioseismology (Howe, 2009).

The first truly systematic observations of the sunspots were undertaken by Samuel Schwabe in the years 1826-43, who eventually discovered the 11-year activity cycle. In 1848 Rudolf Wolf improved the method of counting sunspots (hence known as the Wolf number) and extended the historical records back to 1755, the beginning of Cycle 1[6]. The sunspot cycles are not strictly regular, and periods were identified when very few sunspots were recorded, the best (but sparsely) known was the Maunder minimum (1645-1715) that contributed to a prolonged decrease of interest in observations of the Sun. Other such minima have been inferred from indirect indicators of solar irradiation (e.g., Charbonneau, 2014).

During every cycle, the sunspots first appear at relatively high solar latitudes, up to $\pm 30°$, and then their positions systematically drift towards the solar equator. This trend has been discovered by Richard Carrington (1861), and its description has been soon refined by Gustav Spörer (hence it is known as the Spörer's law). The distribution of sunspot numbers on the diagram of time (on the scale of years) vs. latitude resembles a sequence of butterflies, one per cycle. Some cycles show a small overlap: when an old cycle is reaching its ends with sunspots close to the equator, a new cycle may already produce sunspot at large latitudes.

Since we have mentioned R. Carrington, it is necessary to describe his most famous discovery, the Carrington event of 1859 (Carrington, 1859). He observed a large group of sunspot when *'... two patches of intensely bright and white light broke out ...'*. He then described simultaneous measurements of local magnetic field that showed *'... a moderate but very marked disturbance ... of short duration ...'*, and in the following night *'... there commenced a great magnetic storm ...'*. Carrington observed a *solar flare*, his sketch shows remarkably realistic white arcs connecting two sunspots belonging to a complex group (an *active region*). The great magnetic storm produced intense aurorae observed across the Earth (as far south as Cuba), and induced strong currents in the telegraph systems, disrupting the service in many locations. When such an event happens in our times (it is only the question of when, not if), the damage to our technological infrastructure (in particular the power grids, communications) will be severe. This aspect of solar influence on the Earth is known as the *space weather*[7].

Magnetic fields of sunspots. The possibility to detect and measure magnetic fields in astrophysical sources came with the discovery of the *Zeeman effect* by Pieter Zeeman in 1896 (Nobel Prize 1902).

---

[6]As of 2022, the Sun is in Cycle 25 that began in 2019.

[7]For more information, see the National Academies report 'Severe Space Weather Events' [https://www.nap.edu/catalog/12507/].

Zeeman effect is the splitting of spectral lines in the presence of sufficiently strong magnetic field. High-resolution spectroscopic observations of the Sun by George Hale indeed showed split lines of various elements in the vicinity of sunspots, indicating magnetic field strengths of $2.6 - 2.9 \, \mathrm{kG}$ (Hale, 1908).

Subsequent observations revealed regularities in the polarization of the magnetic field (orientation of its line-of-sight component determined from the circular polarization of secondary lines) (Hale et al., 1919). Yet another fact about sunspots is that, unless they belong to a complex group, they typically appear in pairs oriented roughly longitudinally. More precisely, the line connecting paired sunspots makes a small angle with the solar equator, this angle is roughly proportional to their solar latitude, reaching $\simeq 10°$ at the latitude of $30°$[8]. The magnetic polarities of paired sunspots are always opposite, which suggests that they are connected by a flux tube, in one sunspot the magnetic flux exits out the Sun, in the other sunsplot it enters into the Sun. The polarities of leading pairs (in the sense of the Sun's rotation) are consistent per N/S hemisphere and per solar cycle, and alternating between the hemispheres and subsequent cycles.

The presence of strong magnetic fields passing through the sunspots explains their reduced temperatures of $T \sim 3000 - 4500 \, \mathrm{K}$, as compared to the standard photospheric $T \simeq 5800 \, \mathrm{K}$. Strong magnetic fields prevent convection at the granular scale to transport heat from the solar interior into the sunspots. Quiet regions of the Sun are characterized by weak magnetic fields with $B \sim 1 - 2 \, \mathrm{G}$.

Modern magnetograms fully confirm the Hale's polarity law. In addition, they show ordered magnetic fields in the polar regions of the Sun (generally difficult to observe), indicating a global dipole magnetic field alternating every 2 cycles (e.g., Charbonneau, 2014). Hence, the magnetic fields of the Sun, both in the tropical latitudes and at the poles, follow a *magnetic cycle* of 22 years. The magnetic cycle is clearly evident in a net magnetic flux $\Psi_B = \oint B_\perp \, \mathrm{d}S$ through either (N/S) solar hemisphere that alternates between positive and negative values. In addition, each hemisphere shows a consistent sign of magnetic helicity transfer $(\mathrm{d}/\mathrm{dt}) \int \vec{A} \cdot \vec{B} \, \mathrm{d}V$, with the N(S) hemisphere showing negative(positive) helicity transfer, regardless of the cycle (Berger & Ruzmaikin, 2000).

High-energy observations of the Sun. Modern observations of the solar activity are focused on the extreme ultraviolet (EUV) band that probes plasma of temperatures reaching $T \sim 10^5 \, \mathrm{K}$, performed by space telescopes like the Solar Dynamics Observatory (SDO, since 2010). In this band, most of the solar surface appears dark, and the active regions are distinctingly bright. Above and between the active regions one can see coronal loops with a fine substructure suggesting magnetic field lines. These coronal loops are constantly variable, occasionally producing flares that result in visible changes in their topology. Substructures and variations are not limited to the active regions, small-scale events are also observed in the quiet solar regions. A recent examples are so-called *campfires*, EUV brightenings observed in the quiet solar chromosphere by a new ESA mission Solar Orbiter (SolO, since 2020, closest approach 0.29 AU).

Solar flares are also associated with high-energy emission in the form of X-rays and gamma-rays. For example, the Sun is monitored by the *Fermi* space telescope in soft (sub-MeV; GBM instrument) and high-energy (sub-GeV; LAT instrument) gamma rays. Many powerful solar flares produce detectable gamma-ray emission, which is a direct evidence for non-thermal particle acceleration. Interesting cases have been found of gamma-ray flares associated with solar flares produced behind the solar limb (thanks to the STEREO satellites), which shows that energetic particles can travel along their coronal loops and impact the solar photosphere at the other footpoint (Pesce-Rollins et al., 2015).

Coronal mass ejections. Some solar flares are associated with dynamical *eruptions* that result in ejection of plasma and magnetic energy from the solar corona, so-called *coronal mass ejections* (CME). The CMEs are not easily visible in the visual or UV bands, but they can be observed with the use of coronographs such as SOHO/LASCO or STEREO. The CMEs travel through the Solar System as major disturbances to the solar wind. Associated with them are high fluxes of *solar energetic particles* (SEP). The CMEs may impact magnetospheres of planets and induce magnetic storms. That was the reason for the connection between a solar flare and a geomagnetic storm in the aforementioned Carrington event of 1859. In the recent past, a comparably powerful CME has been produced in July 2012, fortunately it completely missed the Earth (Baker et al., 2013).

---

[8]This is known as the Joy's law after Alfred Joy, a co-author of Hale et al. (1919).

Solar eruption mechanism. A standard model of solar flares and solar eruptions involve coronal loops attached to the solar photosphere. Some complexity is taken into account, e.g., twisted flux tubes or nested field loops. Gradual evolution of these loops may lead to the formation of thin current layers, sites of magnetic reconnection. Reconnection results in localized plasma heating and particle acceleration, it also drives outflows, one directed down to the photosphere, the other directed up to the space (this one generates a CME). Once reconnection becomes fast and efficient, the evolution of the coronal loop accelerates and becomes non-linear (erupts). The main difficulty is to explain the trigger mechanism, as the stability of given magnetic configuration (a critical 'point') is a multi-scale problem. Recent numerical simulations with very high resolution (adaptive mesh refinement) claim to reproduce such a trigger in the ideal MHD with only numerical diffusivity (Jiang et al., 2021).

Solar corona. Solar corona appears as a faint white glow surrounding the Sun during the total solar eclipses. Solar eclipses have been used historically as opportunities to learn about the nature of the corona, and still provide the most detailed images. The first spectroscopic observations of the corona during total eclipses led to the discovery of *helium* (Janssen 1868) and *coronium* (Young 1869, Harkness 1869). While helium turned out to be a new fundamentally important element, the coronium has been a mystery until its $530 \ \mathrm{nm}$ line has been identified as highly ionized iron Fe XIV (Grotrian 1939, Edlén 1943). Such extreme ionization state implies temperatures of the order $\sim 10^6 \ \mathrm{K}$, which posed a serious theoretical problem of *coronal heating*. This problem remains unsolved, and proposed solutions can be grouped into two categories: MHD waves (AC - alternating current) and magnetic reconnection (DC - direct current). All solutions postulate that the source of energy for coronal heating must be the energy of magnetic fields crossing the solar surface. The key challenge is to provide observational evidence that either mechanism can transfer and deposit energy across the corona at a sufficient rate. For example, the solar flares are only the most powerful dissipation events located relatively low in the solar atmosphere, there is evidence for many more small-scale dissipation events (known under different names: nanoflares, Ellerman bombs, campfires) that overall can deposit more heat to the corona, however, the combined effect of observable events is insufficient at least by order of magnitude (e.g., Purkhart & Veronig, 2022).

Two main structures can be distinguished in the solar corona: *helmet streamers* located over low and middle solar latitudes, consisting of closed but sharply elongated magnetic loops, and *coronal holes* (so called because these regions are dark in EUV images) located over the high solar latitudes (the polar regions), consisting of open, roughly dipolar magnetic field lines. The extent of streamers/holes depends on the solar cycle, during the solar minima the coronal holes are much more extended, during the solar maxima they are very limited. Recall that the polar dipole magnetic field shown by the magnetograms is alternating with the 22-year magnetic cycle, but is shifted in phase so that it achieves maximum magnitudes during the solar minima. Note that any coronal heating mechanism must operate in both regions.

Solar wind. The first evidence that the direct influence of the Sun on the Solar System goes beyond its gravity and electromagnetic radiation came from observations of cometary tails. A typical comet produces two tails: a brighter *dust tail* and a fainter *gas tail* that points straight away from the Sun. It was first suggested by Biermann (1951) that the production of ionized gas tails requires a stream of gas particles propagating from the Sun at velocities $\sim 10^3 \ \mathrm{km/s}$. This motivated Parker to consider how can such particles be accelerated, noting that even for the temperature of $\sim 3 \ \mathrm{MK}$ the thermal velocity of particles in the solar corona is $\sim 250 \ \mathrm{km/s}$ (Parker, 1958). The mechanism accelerating the solar wind is still unknown, but it is likely related to the coronal heating mechanism.

Parker argued that ionized gas streaming outwards radially (the solar wind) would drag solar magnetic fields to the interplanetary space, eventually forming a spiral structure (known as the *Parker's spiral*). Such magnetic fields exert a torque on the Sun, potentially braking down its rotation. Parker estimated the braking time scale for the entire Sun as $\sim 30 \ \mathrm{Gyr}$ (a surprisingly accurate value despite assuming $\sim 100\times$ higher gas density), deeming it 'not serious'. The average mass loss of the Sun due to the solar wind is $\sim 3 \times 10^{-14} \ \mathrm{M_\odot/yr}$, and about twice more mass is lost due to nuclear reactions. At the distance of $1 \ \mathrm{AU}$, the typical density of the solar wind is $n \sim 5 \ \mathrm{cm^{-3}}$ and the typical magnetic field strength is $B \sim 50 \ \mu\mathrm{G}$, both subject to very strong variations.

The structure of the solar wind away from the ecliptic plane has been probed by the *Ulysses* mission. At

low latitudes, the solar wind has typical velocities $\lesssim 500 \text{ km/s}$ (with strong variations) and is known as the *slow solar wind*. At high latitudes, the typical velocity is $\sim 700 \text{ km/s}$ (with weak variations) and is known as the *fast solar wind*. There is a clear connection between the slow solar wind and the helmet streamers, and between the fast solar wind and the coronal holes. The angular extension of the slow solar wind is modulated by the solar activity cycle.

In recent years, the inner regions of the solar wind have been probed by the *Parker Solar Probe*, which aims to gradually approach the Sun to a distance as short as 0.046 AU ($9.9 \ R_\odot$), where it will attempt to probe the *Alfvén surface* at which the solar wind becames super-Alfvénic. The Parker Solar Probe has unexpectedly discovered a new type of magnetic structure called *magnetic switchbacks*, localized field reversals detected at the distances of $\sim 0.2 \text{ AU}$ in sections of the solar wind that can be connected to the *equatorial coronal holes* (Bale et al., 2019). Magnetic switchbacks are unknown at 1 AU distances, hence they must be smoothing due to magnetic tension. Their presence is interpreted as evidence for intermittent small-scale dissipation events that may be responsible for solar wind acceleration.

5   Stars

Stars other than the Sun display various signs of magnetic activity. Because of the much greater distances, it is very difficult to obtain their resolved images. Nevertheless, large numbers of stars reveal the variety and statistical properties of possible activities, which is very useful for constraining general models.

Stellar flares.   Stellar flares are direct analogues of the solar flares. They can be observed photometrically in the visual light, large databases of them have been collected already in the 1970s. Typical stellar flare has a duration of a few minutes and may significantly exceed the steady emission of its star.

Modern massive surveys of stellar photometry like Kepler or TESS detect large numbers of flares in all types of stars. For example, a recent analysis of the TESS data employing machine learning identified almost 1 million flares from 160 thousands of stars (Feinstein et al., 2022). Their energy distribution is a power law $\mathrm{d}N/\mathrm{d}E \propto E^{-p}$ with the index $p \simeq 1.4$, consistent with the prediction of the concept of *self-organized criticality*. This is a very general physical principle applicable to any dissipative dynamical systems. A system is the state of self-organized criticality may generate dissipation events of unpredictable scale. Examples include: sand piles where addition of a single grain may generate a collapse, snowy slopes that may generate an avalanche, strained fault zones between tectonic plates that may generate an earthquake, a dry forest that may generate a fire, a moist cloud that may generate rainfall, ecological stress that may bring a species to collapse or extinction, heavy traffic on a highway that may generate a traffic jam, chaos in the financial markets that may generate a stock exchange crash, etc. In the particular case of solar and stellar flares, it is the accumulation of magnetic energy in the twisted coronal loops that may lead to local instabilities that trigger dissipation in the form of magnetic reconnection, which converts the magnetic energy to the energy of flares.

Radio and X-ray emission.   Like the Sun, other stars emit detectable radio and X-ray emission. The radio/microwave emission is interpreted as synchrotron emission from energetic particles trapped in the magnetized corona, and the X-ray emission is interpreted as the thermal emission from the million-K corona. Since both of these bands probe the corona, they can be expected to be correlated, and in fact they are linearly proportional over many decades in luminosity, when comparing data from individual solar flares and many types of stars. This is known as the Güdel-Benz relation (Güdel & Benz, 1993).

Starspots.   Like on the Sun, dark spots known as the *starspots* are inferred observationally on some other stars. Like sunspots, these are regions of significantly reduced effective temperature. Except that starspots that are the easiest to detect are much larger than the sunspots. An extreme example is that of the giant star HD 12545, which shows a huge spot that is several time larger than the Sun, and occupies a large fraction of one hemisphere of its star (Strassmeier, 1999). In the 1990s starspots were being detected using the *Doppler imaging* technique, which reconstructed images of the stellar surface from distorsions of spectral lines measured at multiple rotational phases. That reconstruction method was subject to some

ambiguity, in particular the latitudinal (north-south) degeneracy. In the last decade, unambiguous images of the stellar surfaces were obtained using interferometric observations in the NIR band (e.g., with the CHARA array, Roettenbacher et al., 2016).

Stellar activity cycles. A moderate sample of stars has been monitored for decades, which allows to probe the existence of activity cycles analogous to that of the Sun. Even having a sufficiently long dataset may not be enough to detect a cycle with confidence. Some stars show more than one period. For low-mass stars (spectral types F to M), the identified cycle periods P_{cyc} relate to the rotational periods P_{rot} like $P_{\mathrm{cyc}}/P_{\mathrm{rot}} \sim 10^2 - 10^3$. Two distinct branches in the P_{cyc} vs. P_{rot} space have been proposed (Saar & Brandenburg, 1999), but they remain controversial (e.g., Boro Saikia et al., 2018).

Internal structure of stars. The nature and origin of stellar magnetic fields depends on the internal structure of stars, in particular on the existence of convectively unstable layers. Most stars belong to the *main sequence*, a well defined region in the observationally determined space of effective temperature vs. luminosity – the *Hertzsprung-Russell diagram*. From the theoretical point of view, the main sequence is determined by the mass. A more massive star is more luminous, hotter; it is also larger and it has a shorter lifetime.

The internal structure of stars is also determined by their masses. *Low-mass stars* with $M \lesssim 1.3 M_{\odot}$, including the Sun, have an outer convective zone and a radiative core. However, *very-low-mass stars* with $M \lesssim 0.35 M_{\odot}$ are entirely convective. On the other hand, *high-mass stars* with $M \gtrsim 1.3 M_{\odot}$ have a convective core and a radiative outer layer.

Low-mass stars. The low-mass stars show abundant signatures of magnetic fields characterized by complex structure and strong variability. The properties of these fields depend not only on the mass, but also on the rotation period. Low-mass stars show a broad range of rotation periods, which can now be determined for tens of thousands of stars from massive surveys like Kepler. For example, the Sun is a relatively slow rotator for its mass (a more typical value is ~ 10 d). The stellar rotation rates are thought to be significantly affected by magnetic braking in the protostellar and early main sequence stages. The relative importance of rotation period $P_{\mathrm{rot}} = 2\pi/\Omega$ can be evaluated with the use of dimensionless parameter called the *Rossby number*, which is the strength ratio of the inertial term of the Euler equation (due to convective motions with characteristic velocity v and length scale L) to the Coriolis force density:

$$Ro \equiv \frac{|(\vec{v} \cdot \vec{\nabla})\vec{v}|}{|2\vec{\Omega} \times \vec{v}|} \sim \frac{P_{\mathrm{rot}}}{4\pi L/v} \,. \tag{5.1}$$

For the Sun the Rossby number is slightly greater than 1, but for rapidly rotating ($P_{\mathrm{rot}} \sim 1$ d) M dwarfs ($M < 0.5 M_{\odot}$) it can be as low as ~ 0.01, which means that convective cells are very strongly distorted by the Coriolis force. In these stars the mean surface magnetic field strengths reach values up to ~ 1.5 kG, almost 3 orders of magnitude stronger than ~ 3 G in case of the Sun. The topology of these fields has been determined as mainly poloidal and axisymmetric. Interestingly, in the regime of intermediate Rossby numbers $Ro \sim 0.1$, the topologies are inferred to be completely different – mainly toroidal and non-axisymmetric (Donati & Landstreet, 2009).

High-mass stars. Among the high-mass stars, signatures of magnetic fields are not abundant. The most important group of high-mass stars with strong magnetic fields are the *peculiar A and B stars* (denoted as Ap or Bp). These stars constitute only a few percent of all A and B stars. The peculiarity refers to the chemical composition, in particular to the overabundance of certain metals.

The first star other than the Sun in which the Zeeman effect was detected was the Ap star 78 Vir (Babcock, 1947), which implied $B \sim 1.5$ kG. That first detection was helped by the alignment of the star's rotation axis with the line of sight, which eliminated rotational broadening of spectral lines. Later on, Ap stars were identified with magnetic field strengths up to $B \sim 30$ kG (HD 215441; Babcock, 1960).

The general properties of magnetic fields in Ap stars are periodic modulations with polarity reversals, consistent with the simple *oblique rotator model*, in many cases dominated by a tilted dipole component

frozen into the star. The chemical peculiarities have been demonstrated to be strictly correlated with the magnetic poles. In most cases there is virtually no variability on the time scales of years to decades.

Star formation.   The process of star formation is very strongly affected by the presence of magnetic field. The starting point is gravitational collapse of dense molecular clouds. The interstellar medium in general is magnetized so strongly that the magnetic energy is roughly comparable to gas pressure and kinetic energy density of turbulent motions, we talk about *equipartition*. The dense *prestellar cores* of the molecular clouds are thought to be *magnetically critical*. This means that for a given magnetic flux $\Phi_{\mathrm{B}} = \pi R^2 B$ one can define a critical mass $M_{\mathrm{crit}} \simeq 0.13 \Phi_{\mathrm{B}}/\sqrt{G}$ (based on a modified virial theorem; Mouschovias & Spitzer, 1976). Exceeding M_{crit} leads to a gravitational collapse, in close analogy to the older concept of the Jeans mass. The magnetic criticality of prestellar cores has been confirmed observationally by detection of Zeeman effect in molecular lines in the radio band (Crutcher, 1999). Typical magnetic field strengths are $B \sim 0.4 \mathrm{\ mG}$ for core radii $R \sim 0.1 \mathrm{\ pc}$.

Star-forming molecular clouds are full of not only magnetic field, but also angular momentum. Typical prestellar core contains $\sim 10^{21} \mathrm{\ cm}^2/\mathrm{s}$ angular momentum per gram of mass (*specific angular momentum* $\delta L/\delta M = r^2 \Omega$). For comparison, typical values of $\delta L/\delta M$ are: $\sim 5 \times 10^{17} \mathrm{\ cm}^2/\mathrm{s}$ for a T Tau type protostar, $\sim 10^{15} \mathrm{\ cm}^2/\mathrm{s}$ for the Sun, and $\sim 10^{20} \mathrm{\ cm}^2/\mathrm{s}$ for the Jupiter. On one hand this shows that the original angular momentum can be preserved mainly in the largest planets. On the other hand, an efficient mechanism is required to reduce the angular momentum of stars, both during and after the protostellar stage. Two such mechanisms can be mentioned: magnetic braking and turbulent viscosity (e.g., from the magnetorotational instability - MRI).

Magnetic braking in the protostellar stage may be induced by two types of magnetic structures. The protostars are thought to have extensive magnetospheres that arrest the accretion disk, forcing the fully ionized gas below a certain radius to accrete along the magnetic field lines, exerting a strong torque. At larger scales, the protostellar accretion disks are threaded by roughly vertical (or shaped like an hourglass) magnetic fields that may be associated with outflows in the form of wind or collimated jets, also exerting a torque.

Not all of the original magnetic flux threading a prestellar core makes it onto the star. Magnetic fields are not well frozen into the gas, because most of this gas is not hot enough or shielded from radiation fields to be fully ionized. When ideal MHD is not satisfied, additional physical effects come into play (Armitage, 2011). An important example of such non-ideal effects is the *ambipolar diffusion*, by which neutral atoms in a weakly collisional plasma slip across the magnetic field lines. This means that, in a collapsing prestellar core and in the outer regions of protostellar disks, the magnetic flux is not efficiently dragged inwards.

Origin of stellar magnetic fields.   On this question there are two competing hypotheses.

- *Fossil field* – magnetic field that we observe today is the result of the star formation process and has been largely preserved since then. The current magnetic strength has been amplified by compression during the gravitational collapse. Certain requirements need to be satisfied: sufficient initial magnetic flux, emergence of stable topology, inefficient resistive or turbulent decay. This hypothesis can explain static and simple fields of magnetic Ap stars, independent of the rotation rate, if only sufficient magnetic flux can make it into the star.

- *Dynamo* – magnetic field that we observe today is being constantly regenerated by motions of conducting plasma. It requires a source of kinetic energy, which can be provided by differential rotation and/or convection (ultimately powered by the heat released in thermonuclear reactions). The magnetic field strength can be limited by various quenching mechanisms. Short-term (possibly cyclic) variability and dependence on the rotation rate are signatures of a dynamo. This hypothesis can explain variable and complex fields of low-mass stars (including the Sun) with outer convective zones or fully convective.

6 Galaxies

We have noted that magnetic fields are important in the process of star formation, that molecular clouds are threaded by significant magnetic fluxes. These findings can be extrapolated to the interstellar medium (ISM) and further to entire galaxies. There is plentiful evidence for magnetic fields both in the Milky Way and in other galaxies.

Polarization signatures of magnetic fields. The primary evidence for the presence of magnetic fields in dilute ISM is from the detection of strongly polarized radiation. Energetic particles (cosmic rays) gyrating about magnetic field lines emit *synchrotron radiation* detectable across the radio band and characterized by strong *linear polarization*. At the emission source, the magnetic vectors of the electromagnetic radiation $\vec{B}_{\rm rad}$ (perpendicular to the electric vectors of radiation that are actually detected) are preferentially aligned parallel to the source magnetic field projected to the observer's plane of the sky $\vec{B}_{\rm src,\perp}$. However, in the presence of a foreground ionized medium with magnetic field component $B_{\parallel}$ parallel to the line-of-sight, the polarization angle is subject to *Faraday rotation* by angle $\phi \simeq {\rm RM}\,\lambda^2$, where λ is the radiation wavelength, and ${\rm RM} = e^3/(2\pi m_{\rm e}^2 c^4) \int n_{\rm e}(r) B_{\parallel}(r)\,{\rm d}r$ is the *rotation measure*. Since the Faraday rotation effect increases strongly with increasing wavelength λ, its measurement (to estimate the foreground $B_{\parallel}$) and correction (to reveal the true directions of $\vec{B}_{\rm src,\perp}$) requires multiwavelength observations. At long radio wavelengths the effect becomes severe, leading to an almost complete depolarization of emitted signals (or conversion to the circular polarization).

Magnetic fields in the Milky Way. Magnetic fields of our Galaxy can be probed by all-sky polarimetric surveys in radio and microwave bands. The *Planck* mission, while focused primarily on the cosmological microwave background (CMB), obtained uniform and sensitive polarimetric all-sky maps at frequencies dominated by the Galactic foreground signals (Planck Collaboration, 2016). In the high-frequency radio band at $30\ {\rm GHz}$, the sky is dominated by the Galactic synchrotron radiation. This emission is concentrated along the inner Galactic disk, where magnetic fields show vertical components forming giant loops, in particular in the northern galactic hemisphere (these are relatively nearby superbubbles like Loop I, foreground with respect to the Galactic center). On the other hand, the outer Galactic disk shows mainly horizontal magnetic fields. In the far infrared band at $353\ {\rm GHz}$, the sky is dominated by the thermal emission from cold Galactic dust. This emission is also polarized, because (at least some) elongated dust grains have a preferential orientation with respect to the local magnetic field. This emission is distributed more uniformly along the Galactic plane and traces different regions of the Galactic disk.

The Faraday rotation measure has been calculated as an all-sky maps based on data from many polarimetric radio surveys performed at different wavelengths, including also point sources like pulsars Oppermann et al. (2012). This map consists of patches of ${\rm RM} > 0$, where $\vec{B}_{\parallel}$ is directed to the observer, and ${\rm RM} < 0$, where $\vec{B}_{\parallel}$ is directed away from the observer. The root-mean-square value along the Galactic equator is $\simeq 200\ {\rm rad/m^2}$. There is a preference for positive ${\rm RM}$ in the western Galactic hemisphere ($l < 0$), and for negative ${\rm RM}$ in the eastern Galactic hemisphere ($l > 0$). This is consistent with the presence of a local toroidal field component oriented to the east ($l \sim 90°$) (Jansson & Farrar, 2012). Additional large-scale structures both along and across the Galactic plane can be correlated with neighbouring Galactic spiral arms.

Typical magnetic field strengths in the Milky Way are $\sim 5\ \mu{\rm G}$, consistent with direct measurements performed by both Voyager probes outside the heliosphere (Beck, 2015).

Magnetic fields in spiral galaxies. The main problem in trying to understand the structure of magnetic fields in the Milky Way is that we are located within the Galactic disk, which is not a good vantage point. Nearby spiral galaxies of large angular diameters are much better targets to obtain an unbiased global picture.

Our neighbour spiral, the *Andromeda galaxy (M31)*, shows radio emission in the form of a ring with reconstructed magnetic field vectors oriented along the ring of radius $\simeq 10\ {\rm kpc}$, indicating the axisymmetric ($m = 0$) toroidal geometry (Beck, 2015). This is rather atypical for other spirals, but this ring in M31 is also

prominent in the far-infrared band, as has been first observed by the *Infrared Space Observatory (ISO)* in 1998. While hidden in the visual band, this is a site of enhanced star formation.

A famous large spiral oriented face-on, the *Whirlpool galaxy (M51)*, shows radio emission well aligned with its two grand spiral arms with plentiful star formation. The reconstructed magnetic field vectors are parallel to the local directions of the spiral arms (Fletcher et al., 2011). They thus show significant *pitch angles* of $\sim 20°$ with respect to the local circular orbits followed by most stars. This is an important indication that global (weakly differential) rotation of the galaxy is rather unimportant in amplifying the galactic magnetic fields (so called $\alpha - \Omega$ dynamo). The global distribution of regular magnetic fields in M51 has been modeled in terms of two geometric components: a disk component with a combination of axisymmetric ($m = 0$) and quadrisymmetric ($m = 2$) spiral structures, and a halo component with bisymmetric ($m = 1$) spiral structure.

A less known face-on spiral galaxy that has been important for studies of galactic magnetism is NGC 6946. This galaxy has multiple prominent spiral arms, but its radio emission is relatively patchy, and is clearly concentrated between the spiral arms (Beck, 2015). One can thus describe these structures as the *magnetic spiral arms*, with the reconstructed magnetic field vectors following their local directions. One of possible explanations why magnetic arms are located between the gaseous arms is the *Parker instability* (see the Theory notes), which makes ordered magnetic fields bouyantly unstable, so that they concentrate in regions of lower gravitational potential.

Some spiral galaxies have their disks oriented edge-on, and they offer an oppportunity to investigate the vertical structure of magnetic fields. High-quality observational data on targets such as NGC 4217, NGC 4666, NGC 5775 have been recently obtained from the CHANG-ES survey on the JVLA (Krause et al., 2020). These data reveal plane-symmetric magnetic structures elevated over the outer disk regions, overall resembling letter X. These structures suggest domination of a quadrupolar component.

Typical total magnetic field strengths (including the turbulent component) are $\sim 10 \ \mu\mathrm{G}$, and up to $\sim 30 \ \mu\mathrm{G}$ in dense spiral arms (Beck, 2015). Ordered magnetic fields can be up to $\sim 15 \ \mu\mathrm{G}$ in the magnetic spiral arms.

Other types of galaxies. *Starburst galaxies* are characterized by intense star formation at the rates order-of-magnitude higher than for standard spirals. A primary example is M82, where strong ($\sim 300 \ \mu\mathrm{G}$) vertical (roughly dipolar) magnetic field has been found to coincide with the base of the outflows driven by the starburst (for recent observations by the SOFIA airborne IR telescope, see Lopez-Rodriguez et al., 2021). Magnetic field strengths of $\sim 30 \ \mu\mathrm{G}$ are being measured in colliding galaxies like the famous 'Antennae' (Basu et al., 2017). The link between magnetic field strength and star formation rate is underlined by a strong observational correlation between radio and far-IR luminosities for various galaxies up to redshift $z \simeq 1.2$, without signs of cosmological evolution (Basu et al., 2015). Significant radio luminosity of relatively young galaxies suggests that the dynamo mechanism of magnetic field amplification must be operating fairly quickly. The origin of galactic magnetic fields, in the absence of nuclear activity, is thus clearly related to the star formation. This is also true for the *elliptical galaxies*: they show little star formation activity ('red and dead') and only very weak radio emission (radio quiet, unless active). It is difficult to observe them, and indeed there are not many such observations, but they typically reveal patches of radio emission that coincide with patches of star formation (see Capetti et al., 2022, for recent results from the LOFAR).

Origin of galactic magnetic fields. It is accepted that galactic magnetic fields must be amplified by a dynamo mechanism. Two main sources of kinetic energy are: the global (weakly differential) rotation of the galactic disk, and turbulent motions in the interstellar medium (ISM). If the dynamo was driven primarily by the disk rotation (the Ω shear mechanism), one would expect small pitch angles for regular magnetic fields (contrary to the observations), and the field amplification would have to be very rapid in terms of galactic rotational periods P_{rot} (galaxies rotate slowly, the Hubble time makes $\sim 50 P_{\mathrm{rot}}$).

The large-scale dynamo process can be significantly accelerated by small-scale turbulence. Two main drivers of turbulent motions have been considered. The first driver is the supernova explosions, a single supernova influences not only a local disk, but also large regions of the galactic halo. It is estimated that the turbulent kinetic energy in the ISM of our Galaxy corresponds to ~ 5000 supernovae. Numerical MHD simulations of a Milky Way size galaxy including the supernova feedback show that $\mu\mathrm{G}$ field strengths can

be produced on Gyr time scales (Butsky et al., 2017). The second driver is the magnetorotational instability (MRI) operating in a galactic disk. It has been proposed that MRI can produce quadrupolar magnetic fields that are observed in edge-on spiral galaxies Kitchatinov & Rüdiger (2004).

A more difficult question is to identify the seed fields for galactic dynamos, and even to estimate their order-of-magnitude strengths.

7 Relativistic jets

Relativistic jets are characteristic features of certain galaxies with an active nucleus, the *active galactic nuclei* (AGN). The properties of relativistic jets will be introduced using the example of M87, one of the best studied AGN, both historically and presently.

7.1 M87

M87 denotes the 87th entry in the catalogue of nebulae compiled by Charles Messier in 1781. It is an elliptical galaxy in the constellation of Vigro, a member of the Virgo Galaxy Cluster. In 1918, Heber Curtis noted *"a curious straight ray lies in a gap in the nebulosity in position angle* $20°$*, apparently connected with the nucleus by a thin line of matter"*. This was the first reported observation of a jet, the position angle is currently given as $288°$ measured from the north to the east, the jet is thus directed WNW. Baade (1956) observed M87 with a polarimeter and found that emission from the jet (specifically from its main kpc-scale knots denoted as A ($12''$ from the nucleus), B and C) is significantly polarized, as opposed to emission from the galaxy. This, together with a distinct blue color of the jet, and recent identification of M87 with a strong radio source Virgo A, suggested that emission from the jet is due to the synchrotron radiation.

The radio source Virgo A is thus a radio galaxy, it extends well beyond the optical galaxy and beyond the optical jet. Its high-quality images obtained by the Very Large Array (VLA) show various levels of detail depending on the observational wavelength $\lambda_{\rm obs}$. At $\lambda_{\rm obs} = 90$ cm, a diffuse structure extending to ~ 100 kpc, consisting of two brighter irregular outer lobes/arms and a fainter halo (Owen et al., 2000). At $\lambda_{\rm obs} = 20$ cm, the inner region extending to ~ 3 kpc is resolved into two inner lobes, the western one fueled by the jet, which appears to lose its collimation beyond knot C and bend to the south. At $\lambda_{\rm obs} = 2$ cm, resolution better than $1''$ is reached ($\simeq 80$ pc at the distance of $D \simeq 17$ Mpc), allowing to probe the transverse structure of the jet, and revealing a number of fainter knots (D, E and F) upstream from knot A. Very Long Baseline Interferometry (VLBI) (e.g., the Very Long Baseline Array – VLBA) at $\lambda_{\rm obs} = 2$ cm achieves resolutions better than 10 mas $= 0.01''$, probing sub-pc scales, but the radio core remains unresolved.

Starting in the 1990s, the jet of M87 has been monitored by the Hubble Space Telescope (HST) at sub-arcsecond resolution. Hubble revealed additional knots (HST-1 ($0.86''$ from the nucleus) and HST-2) upstream from knot D, and detected *apparently superluminal motions*, $v_{\rm app} \sim (5-6)c$, of substructures within knots HST-1, D and E (Biretta et al., 1999). This means that the jet of M87 is *relativistic*, i.e., that it propagates with subluminal but very close to c speeds $v_{\rm j}$ corresponding to the Lorentz factor $\Gamma_{\rm j} = [1 - (v_{\rm j}/c)^2]^{-1/2} \geq v_{\rm app}/c$.

About the same time, interferometric radio observations with the VLBA performed at a shorter wavelength of $\lambda_{\rm obs} = 7$ mm achieved a mas resolution, revealing the jet collimation zone with opening angle of $\simeq 60°$ at projected distance of ~ 0.04 pc from the still unresolved core (Junor et al., 1999). The M87 jet has been monitored with the 7 mm VLBA over two decades (Walker et al., 2018), the results of this monitoring have been presented as a movie[9].

Also around that time, the Chandra X-ray Observatory (CXO) provided sub-arcsecond resolution in the X-ray band. Chandra can observe the diffuse emission associated with the outer radio lobes, the hot galactic halo, and the jet, including the HST-1 knot resolved from the nucleus. Soon after the HST-1 knot started to be monitored in X-ray, optical and radio bands, it produced a spectacular multi-year outburst. At the peak brightness in 2005, it exceeded the nucleus by more than factor 10 in the X-ray band (Harris et al., 2009), and by more than factor 3 in the optical band (Madrid, 2009). Comparing the X-ray, optical and

---

[9] https://www.aoc.nrao.edu/~cwalker/M87/

radio light curves of HST-1 (Harris et al., 2009), one can note a very strong correlation with simultaneous peaks, but also systematic trends with the photon energy. The outburst appears to be the sharpest in X-rays. While the flux-raising profiles are similar, the flux decay is clearly faster for higher photon energy. This is consistent with the baseline scenario, in which both radio, optical and X-ray emissions are due to synchrotron radiation of electrons with very different energies E. For fixed magnetic field strength (here estimated at $B \simeq 0.6$ mG), the synchrotron cooling time scale should scale like $t_{\rm syn} \propto E^{-2}$, and this is exactly what is observed. In 2005, M87 was detected as a source of TeV gamma rays with strong variations on the time scale of days (Aharonian et al., 2006). Were these produced in the nucleus or in the HST-1? Unfortunately, gamma-ray observatories like H.E.S.S. have angular resolution of $\sim 0.1°$, insufficient even to resolve the jet from the inner lobes. The nuclear hypothesis is supported by the fact that the variability time scale corresponds to a few light crossing times of the gravitational radius of the central black hole (see below), and by the fact that further gamma-ray flares from M87 have been detected in the following years, after HST-1 decayed by more than factor 10 in the X-rays. The HST-1 hypothesis is also challenging from the theoretical point of view, since M87 is not a blazar (the jet viewing angle is estimated at $\simeq 18° > 1/\Gamma_{\rm j}$ for $\Gamma_{\rm j} > 5$), its emission should be relativistically deboosted, but the same difficulty applies to the X-ray outburst of HST-1. The nuclear hypothesis appears to be more likely, but the origin of at least the 2005 gamma-ray flares in the HST-1 cannot be ruled out.

High-quality radio observations of the M87 jet are continuing, advances in the sensitivity allow to obtain detailed maps of linear polarization and Faraday rotation measure. Polarization magnetic vectors (perpendicular to the polarization electric vectors) show that magnetic fields are generally oriented along the jet, with notable exceptions of knots A and C, where it is perpendicular to the jet, most likely due to compression by shock waves (Algaba et al., 2016). Recent results from the upgraded VLA (now called the Jansky VLA - JVLA) revealed a double helical structure of the jet between knots D and A (Pasetto et al., 2021). Such an ordered structure is rather unexpected at kpc distance scales[10], it is an evidence for very robust stability of ordered magnetic fields in relativistic jets.

A further progress in angular resolution has been made by performing VLBI observations at $\lambda_{\rm obs} = 3.5$ mm (Hada et al., 2016; Kim et al., 2018). This allowed to obtain a resolution of up to $\simeq 50\ \mu$as, corresponding to a linear size of $\simeq 13R_{\rm g}$[11]. The jet collimation zone has been resolved further to the opening angle of $\sim 120°$, but the core remained unresolved, with the jet/core brightness ratio of ~ 25.

Those observations have been the final step before the historical breakthrough achieved by the Event Horizon Telescope (EHT), a global VLBI network observing at $\lambda_{\rm obs} = 1.3$ mm. They observed M87 at the angular resolution of $\simeq 20\ \mu$as and resolved the core (now called M87*) into a ring of angular diameter $\simeq 42\ \mu$as that corresponds to $\simeq 11R_{\rm g}$ (Event Horizon Telescope Collaboration, 2019.I). They did not detect the jet outside the ring because they did not achieve the required 1:25 contrast. The ring is not of uniform brightness, it is generally brighter along the southern side. There is possibly a substructure along the ring[12] that would consist of a proper crescent in the SSE - WSW sector and an ESE hotspot (Nalewajko et al., 2020). Emission from the proper crescent can be explained by plasma orbiting the black hole along its equatorial plane, assuming that the spin vector is aligned with the WNW jet axis. Emission from the ESE hotspot is unexpected in such a basic scenario, if the emitting plasma is distributed axisymmetrically, it should rather be a temporary localized fluctuation, such fluctuations are common in the GRMHD simulations of black hole accretion flows (Event Horizon Telescope Collaboration, 2019.V). The M87* ring emission has also been shown to be partially polarized (Event Horizon Telescope Collaboration, 2021.VII). Emission from the proper crescent shows linear polarization degrees up to $\sim 15\%$ with polarization vectors aligned in a spiral pattern that has been likened to the Parker spiral in the Solar System (Punsly & Chen, 2021). However, emission from the ESE hotspot appears to be unpolarized, which would support its distinct nature (Nalewajko, 2021).

---

[10]Knot E is located at the *projected* distance from the nucleus of ~ 0.5 kpc. Accounting for the viewing angle of $\simeq 18°$, this corresponds to an *unprojected* distance of ~ 1.6 kpc.

[11]The mass of the central black hole of M87 has been controversial, until 2019 two estimates of 3 and 6 billion solar masses have been cited, based on two independent methods. This effected all estimates of lengths in terms of the gravitational or Schwarzschild radii. The higher mass estimate has been confirmed by the EHT observations (Event Horizon Telescope Collaboration, 2019.I) that found $M \simeq 6.5 \times 10^9 M_\odot$, for which $R_{\rm g}$ has an angular size of $\simeq 4\ \mu$as and light-crossing time scale of $\simeq 9$ h.

[12]The existence of a substructure in the ring image of M87* has not confirmed by the EHT Collaboration, since different image reconstruction methods yield results that differ in details.

7.2 Active galactic nuclei

M87 is just one example of a galaxy with an *active galactic nucleus* (AGN). It is also a *radio galaxy*, but not a particularly luminous one. Really luminous AGN are observed at cosmological distances, they are called the *quasars*, because they appeared as point sources in the optical band when they were discovered in the 1960s. The first identified quasar was 3C 273, in which emission lines are redshifted by factor $(1 + z)$ with $z \simeq 0.158$ (Schmidt, 1963). Quasars reside in large elliptical galaxies, the emission of which is hard to detect because it is outshined by the nucleus. High-quality observations of 3C 273 by the Hubble Space Telescope revealed that it is not a point source, but it has a kpc-scale jet pointing SW. This jet has been previously detected in radio by the VLA and subsequently in the X-rays by Chandra and in the IR by Spitzer. It is thus a truly multiwavelength jet, although its appearance is very different in different bands: in the X-rays it is brightest at the inner end, in the radio it is brightest at the outer end (Uchiyama et al., 2006).

Radio galaxies can be classified according to their overall appearance in radio into two Fanaroff-Riley (FR) type (Fanaroff & Riley, 1974): FR I types (including M87) shows peak radio brightness near the center, along the inner jets that visibly weaken (subject to bending) due to dissipation and diffuse into low-brightness radio lobes; FR II types (exemplified by Cygnus A) shows peak radio brightness at two opposite edges in the form of hotspots connected with the fainter nucleus by even fainter straight jets (suggesting little dissipation) and fuelling radio lobes flowing in a direction opposite to the associated jet. The FR II radio galaxies are associated with quasars (radiatively thick accretion disks), and are systematically more luminous than the FR I types associated with low-luminosity AGN (LLAGN; with radiatively thin accretion flows).

The nearest AGN is not M87, but FR I radio galaxy Centaurus A ($\simeq 4$ Mpc) associated with elliptical galaxy NGC 5128 with a prominent dust lane. This dust obscures the nucleus in the optical and soft X-ray bands, while two radio lobes extend roughly perpendicular to the lane, the northern one fueled by a jet bright in the radio and X-rays, but not visible in the optical. The radio lobes are surrounded by faint shells of X-ray emission. The multiwavelength combined image of Cen A has a striking similarity (only at much larger scale) to the famous cartoon of the AGN unification model of Urry & Padovani (1995). The main feature of every AGN is a supermassive black hole (SMBH; $M_{\mathrm{BH}} \sim 10^{7-9} M_\odot$) that actively accretes matter, typically from a dusty torus, sometimes in the form of an accretion disk. Depending on the obscuration of the nucleus by dust, which in the case of a torus is primarily the function of viewing angle, AGN are classified into type 1 (not obscured) and type 2 (obscured). Roughly 10% of AGN produce two jets directed oppositely (perpendicular to the equatorial plane of the accretion flow) that inflate radio lobes, these are known as *radio loud* (the remainder are known as *radio quiet*). Radio loud AGN can be further classified into *blazars* and radio galaxies, depending on the viewing angle of the jet, as will be explained below.

7.3 Jets from stellar mass objects

Relativistic jets are also produced by stellar binaries, in which one object is compact (neutron star or stellar-mass black hole) accreting matter from the companion. A well known example are two jets in the X-ray binary SS 433, the dynamics of which has been densely monitored in a VLBA campaign[13]. The apparent speed of jet features in SS 433 is clearly subluminal with $v_{\mathrm{app}} \sim 0.25c$, but in the case of X-ray binary GRS 1915+105 it is transluminal with $v_{\mathrm{app}} \sim c$ (Mirabel & Rodríguez, 1994; Fender et al., 1999), which has been named a *microquasar*. It has therefore been presumed that relativistic jets are produced by the same mechanism at very different scales: supermassive ($\sim 10^9 M_\odot$) black holes in AGN, and stellar-mass ($\sim 10 M_\odot$) black holes in microquasars (and gamma-ray bursts, GRBs) (Mirabel & Rodríguez, 1998). The vastly different black hole masses imply in particular vastly different time scales on which the jets evolve.

7.4 Blazars

For AGN that produce relativistic jets (radio loud), the apparent luminosity depends very sensitively on the viewing angle. If the observer is located within the Dopppler cone of one of the jets, the luminosity of radiation from that jet will be boosted by factor $\mathcal{D}^4$, where $\mathcal{D} \sim 10$ is the relativistic Doppler factor (see the Theory notes). Consequently, since jets can be very powerful (comparable with the Eddington luminosity)

---

[13] https://www.nrao.edu/pr/2004/ss433/

and dissipate their energy efficiently, their emission easily dominates that of the entire host galaxy, including the quasar component (accretion disk). Observationally, blazars are characterized by very broad *spectral energy distributions* (SED), extending across the entire electromagnetic spectrum from the radio to the gamma rays. They are also notoriously variable in time, especially in the gamma-ray band. This variability is unpredictable (stochastic) and occurs on a broad range of time scales, from years down to minutes (which is shorter than the light-crossing time – a few hours – of the SMBHs). The shortest time scales are measured during occasional very bright flares, detected both by ground-based Cherenkov telescopes like *H.E.S.S.* (most sensitive in the TeV band) (e.g., Aharonian et al., 2007), and by the space-based pair-conversion telescopes like *Fermi* (most sensitive in the GeV band) (e.g., Ackermann et al., 2016). Such rapid gamma-ray flares pose a unique theoretical problem that sparked interest in relativistic magnetic reconnection.

The SED of blazars consist of two main non-thermal components: the low-energy component (radio - UV/X-ray) is recognized as the synchrotron emission (emission of relativistic electrons gyrating in magnetic field); the high-energy component (X-ray - gamma-ray) could be either due to inverse Compton (IC) scattering (of soft radiation fields by energetic electrons) or due to hadronic processes (particle cascades or synchrotron emission due to relativistic protons) (e.g., Sikora et al., 2009).

There are two major subclasses of blazars. One is known as the *flat spectrum radio quasars* (FSRQ): these are more luminous ($\sim 10^{48}$ erg s^{-1}), their high-energy component peaks in the MeV-GeV range of photon energies and dominates over the low-energy component that extends only to the UV band; in the optical band they show broad emission lines and sometimes the accretion disk emission. The other subclass is known as the *BL Lacertae objects* (BL Lacs): these are less luminous ($\sim 10^{45}$ erg s^{-1}), their high-energy component peaks in the GeV-TeV range and is comparable with the low-energy component that extends to the X-ray band; in the optical band they show very weak or no emission lines (unknown spectroscopic redshift). Across these two subclasses, the luminosity of the synchrotron component L_{syn} appears to be anti-correlated with its peak frequency ν_{syn} (spanning the range of $10^{13} - 10^{17}$ Hz), forming so-called *blazar sequence* (Fossati et al., 1998). The synchrotron peak frequency also appears to be correlated with the apparent speed β_{app} of radio jet features (reaching higher values up to ~ 30 for the FSRQs, Lister et al. 2019) and with the optical polarization degree (reaching higher values up to $\sim 30\%$ for the FSRQs, Angelakis et al. 2016).

Modeling of the blazar SEDs can be used to estimate parameters of relativistic jets, including the magnetic field strength. This is more straightforward in the case of FSRQs, where the leading interpretation of the high-energy component is the IC scattering of external radiation fields (originating outside the jet; Sikora et al. 1994). Assuming that both of the main SED components are produced by the same population of energetic electrons, their luminosity ratio can be expressed as $L_{\mathrm{syn}}/L_{\mathrm{IC}} \simeq u'_{\mathrm{B}}/u'_{\mathrm{ext}}$, were $u'_{\mathrm{B}} = B'^2/8\pi$ is the co-moving magnetic energy density, and u'_{ext} is the co-moving energy density of the external radiation. The latter can be related to the accretion disk luminosity L_{acc} (which may be observed directly in the optical band) via $u'_{\mathrm{ext}} \sim \xi \Gamma_{\mathrm{j}}^2 L_{\mathrm{acc}}/(4\pi c r_{\mathrm{ext}}^2)$, where $\xi \sim 0.1$ is the geometric covering factor and r_{ext} is the characteristic radius of the external radiation source. Two particular sources of external radiation can be considered: (1) broad emission lines (BEL) of typical photon energy $E_{\mathrm{BEL}} \sim 10$ eV produced in a broad line region (BLR) of typical radius $r_{\mathrm{BLR}} \sim 0.1 L_{\mathrm{acc},46}^{1/2}$ pc; (2) hot dust radiation (HDR) of typical photon energy $E_{\mathrm{HDR}} \sim 0.3$ eV produced in a dusty torus (DT) of typical radius $r_{\mathrm{DT}} \sim 2.5 L_{\mathrm{acc},46}^{1/2}$ pc, where $L_{\mathrm{acc},46} = L_{\mathrm{acc}}/(10^{46}$ erg s$^{-1})$. Both scenarios predict comparable magnetic field strenghts of $B' \sim 0.4$ G at the distance of $r = 1$ pc (for $L_{\mathrm{IC}}/L_{\mathrm{syn}} \sim 10$ and $\Gamma_{\mathrm{j}} \simeq 15$), which corresponds to the magnetic jet power of $L_{\mathrm{B}} = \pi R^2 \Gamma_{\mathrm{j}}^2 c u'_{\mathrm{B}} \sim 5 \times 10^{45}$ erg s^{-1} (for $R \simeq r/\Gamma_{\mathrm{j}}$).

In the case of BL Lacs the standard SED models interpret the high-energy component as Comptonization of synchrotron radiation internal to the jet (Synchrotron Self-Compton, SSC), leading to two issues. One issue is that the magnetic field strength is degenerate with the Doppler factor, hence usually there is no unique solution. The other issue is that the inferred magnetic energy densities are very low compared to the energy densities of the energetic electrons $u'_{\mathrm{B}} \ll u'_{\mathrm{e}}$, i.e., the magnetic fields are strongly sub-equipartition (Tavecchio & Ghisellini, 2016). Equipartition ($u'_{\mathrm{B}} \sim u'_{\mathrm{e}}$) is a common assumption used to interpret the intensities of radio sources. It is often expected that plasmas tend to relax towards equipartition: super-equipartition fields would bulk-accelerate plasma; sub-equipartition fields may be amplified by dynamo mechanisms.

Another effect that can be used to independently estimate the magnetic field strength in relativistic jets is the *synchrotron self-absorption* (SSA). Compact emitting regions (of radius R) absorb radio waves longer than a characteristic frequency that can be expressed as $\nu'_{\mathrm{SSA}} \simeq (1/3)(eB'/m_{\mathrm{e}}^3 c)^{1/7} L'^{2/7}_{\mathrm{syn}} R^{-4/7}$ in the jet co-moving frame (Nalewajko et al., 2014). In luminous FSRQs, the SSA may produce a spectral cut-off in the millimeter band at HDR distances, shifting to the far/mid-IR band at BLR distances. In radio VLBI images of blazar jets, the SSA creates a photosphere that appears as the brightest feature of the image - the *radio core*. VLBI images obtained at different frequencies show very small but measurable shifts Δ in the position of the radio core along the jet (once the optically thin features are properly aligned, e.g., Fromm et al., 2013), scaling like $\Delta \propto \nu^{-1}$ in conical jets. The magnetic field strength is expected to scale like $B' \propto \Delta^{3/4}$, hence radio core shift measurements allow to estimate the jet magnetic fluxes for a substantial sample of blazars (Zamaninasab et al., 2014). These magnetic fluxes have been demonstrated to be consistent with the prediction of the *magnetically arrested disk* (MAD) model of accretion onto the SMBH.

8 Particle acceleration

8.1 Collisionless shocks

The shock jump equations assume that ideal MHD is satisfied at both sides of the shock front, and that the parameters jump sharply. This is a severe simplification. In reality, when a uniform flow is suddenly disrupted, it takes some time to achieve a new equilibrium. This can happen quickly in a strongly collisional fluid. However, many astrophysical environments are characterized by low particle density and infrequent collisions. In the limit of collisionless ionized plasma, particle interactions will be primarily electromagnetic, introducing additional length scales, including the gyroradius in the presence of magnetic fields. Shocks can still form in such situations, but they have a complex structure, and will be mediated by many plasma effects.

The most important aspect of collisionless shocks is that they can be efficient sites of non-thermal particle acceleration. In the process known as the *diffusive shock acceleration* (DSA; Blandford & Eichler, 1987), a particle can be energized every time it crosses the shock front. Some particles may cross the shock front multiple times and will gain a lot of energy. If every energy gain scales like $\Delta E \sim E$, the particle energy will increase exponentially, realizing the idea of the *first-order Fermi mechanism* (Fermi, 1949).

While particles can easily cross the shock front from the upstream to the downstream, it is more difficult to make them return to the upstream region. In the presence of uniform magnetic field, a particle will be tied to move mainly along the local field line. In the case of parallel magnetic field, a particle can travel both ways without much difficulty. In the case of perpendicular magnetic field, a particle will be carried downstream away from the shock, without any chance of returning. The intermediate case of oblique magnetic fields is the subject of Problem 6 (see the Theory notes).

Even completely unmagnetized plasmas can generate magnetic field around the shock front, which is possible because a fraction of particles (ions in electron-ion plasmas) are reflected off the shock front and generate current densities in the near upstream region, where counterstreaming instaiblities (in particular the Weibel instability) form current filaments that are sources of small-scale magnetic fluctuations. Such fluctuations, present both upstream and downstream, are important for scattering the particle trajectories, which allows them to change their velocity relative to the shock front and for some of them to make the multiple crossings and achieve very high energies (Spitkovsky, 2008).

Particle acceleration at collisionless shocks can be probed in different astrophysical environments. Among the planetary bow shocks, forming in the solar wind just before impacting a planetary magnetosphere, that of Saturn is particularly strong, and has been probed directly by the Cassini mission (Masters et al., 2013). Supernova remnants are the key sites of acceleration of galactic cosmic rays, reaching energies up to $\sim \mathrm{PeV}$. Strong shock waves can be observed directly along their edges, and energetic X-ray emission resolved by Chandra can be pinpointed to them, allowing to constrain the particle acceleration efficiency (Uchiyama et al., 2007). Strong collisionless shocks have also been identified along the outer edges of radio halos in galaxy clusters, a well known example is the 'Sausage' relic in cluster CIZA J2242.8+5301

(van Weeren et al., 2010).

Relativistic shocks are expected to be present in the pulsar wind nebulae (PWNe), in AGN jets and in gamma-ray bursts (GRBs). The best known PWN, the Crab, shows a ring structure resolved by *Chandra* and *Hubble* space telescopes that surrounds the centrally positioned pulsar (Hester et al., 2002). This ring is associated with the termination shock that limits an ultra-relativistic wind emerging from the pulsar magnetosphere beyond the much more compact light cylinder.

A   Problems

Problem 2 (Elsasser number).   Elsasser number Λ is the strength ratio of the Lorentz force density $\vec{f}_{\mathrm{L}} = (\vec{j} \times \vec{B})/c$ to the Coriolis force density $\vec{f}_\Omega = 2\rho\vec{\Omega} \times \vec{v}$. Create a scatter diagram of equatorial dipole magnetic field strength at the surface B_{s} vs. the rotation period P for planets and moons. Where possible, indicate also the dipole magnetic field strength scaled to the core radius B_{c}. What values of Λ are inferred? For magnetic diffusivity, assume $\eta \sim 10^4$ cm^2/s for liquid iron, $\eta \sim 10^5$ cm^2/s for metallic hydrogen, and $\eta \sim 10^6$ cm^2/s for liquid CNO.

Solution to Problem 2.   The Elsasser number can be evaluated approximately as:

$$\Lambda = \frac{|\vec{f}_{\mathrm{L}}|}{|\vec{f}_\Omega|} = \frac{|(\vec{j} \times \vec{B})/c|}{|2\rho\vec{\Omega} \times \vec{v}|} \simeq \frac{jB}{2c\rho\Omega\mathrm{v}} \ . \tag{A.2}$$

Substituting the angular velocity $\Omega = 2\pi/P$ and the current density

$$j \simeq \sigma E \simeq \frac{\sigma B\mathrm{v}}{c} = \frac{cB\mathrm{v}}{4\pi\eta} \ , \tag{A.3}$$

one obtains $\Lambda \simeq B^2 P/(16\pi^2\eta\rho)$.

Table 1: Mean equatorial surface magnetic field strength B_{s} (from the dipole moment or its upper limit), sidereal rotation period P, relative radius of the liquid core (or other convective region) $R_{\mathrm{c}}/R_{\mathrm{s}}$, and magnetic diffusivity η for planets and selected moons of the Solar System. Data marked in red are approximate estimates that were not mentioned during the lecture.

		B_s[G]	P[d]	R_c/R_s	η[cm^2/s]
Earth	dipole	0.3	1.0	0.55	1.0e4
Moon	ul	2.0e-6	27.3	0.20	1.0e4
Mercury	dipole	0.002	58.6	0.85	1.0e4
Venus	ul	2.0e-5	243.0	0.58	1.0e4
Mars	ul	0.0001	1.03	0.54	1.0e4
Jupiter	dipole	4.17	0.41	0.80	1.0e5
Ganymede	dipole	0.0072	7.2	0.20	1.0e4
Saturn	dipole	0.21	0.44	0.50	1.0e5
Uranus	dipole	0.23	0.72	0.80	1.0e6
Neptune	dipole	0.13	0.67	0.80	1.0e6

Data for planets are summarized in Table 1. The relative core radius can be used to scale the surface dipole magnetic field strength to the core radius $B_{\mathrm{c}} = B_{\mathrm{s}}(R_{\mathrm{c}}/R_{\mathrm{s}})^{-3}$. In addition, one should adopt an approximate value for the core density. Here, we adopt $\rho \simeq 10$ g/cm^3, which is valid for the iron core of the Earth. This solution can be improved by adopting a lower density for the convective layers of the gas giants.

The results are illustrated in Figure 1. Possible conclusions that can be drawn from this plot are:

- The inferred values of the Elsasser number are $\Lambda \sim 10^{-14} - 10^{-4}$ at the surfaces, and $\Lambda \sim 10^{-11} - 3 \times 10^{-4}$ in the cores.
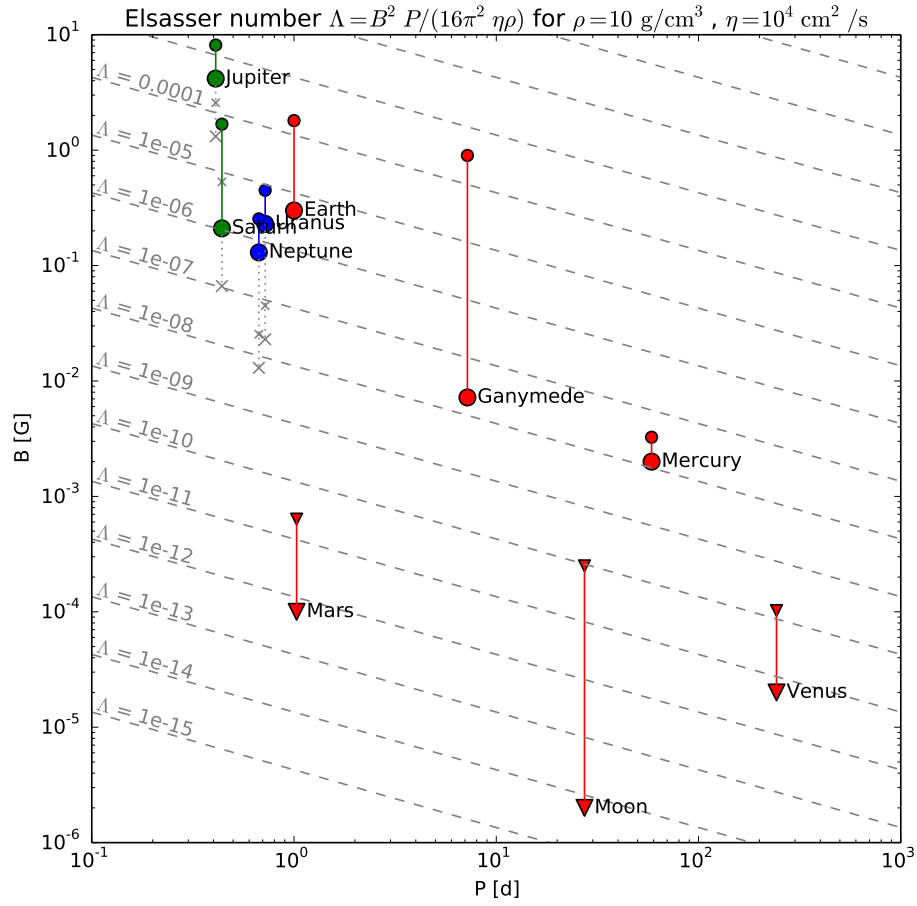
Figure 1: Solution to Problem 2. Scatter diagram showing surface magnetic field strength B_s (large circles) and core magnetic field strength B_c (small sircles). The symbol color indicates the adopted magnetic diffusivity value η: red $- 10^4$ cm^2/s (liquid iron), green $- 10^5$ cm^2/s (metallic hydrogen), blue $- 10^6$ cm^2/s ('CNO ocean'). The gray dashed lines indicate the Elsasser number values Λ for $\eta = 10^4$ cm^2/s. The gray crosses indicate corrections to the value of Λ for $\eta > 10^4$ cm^2/s.
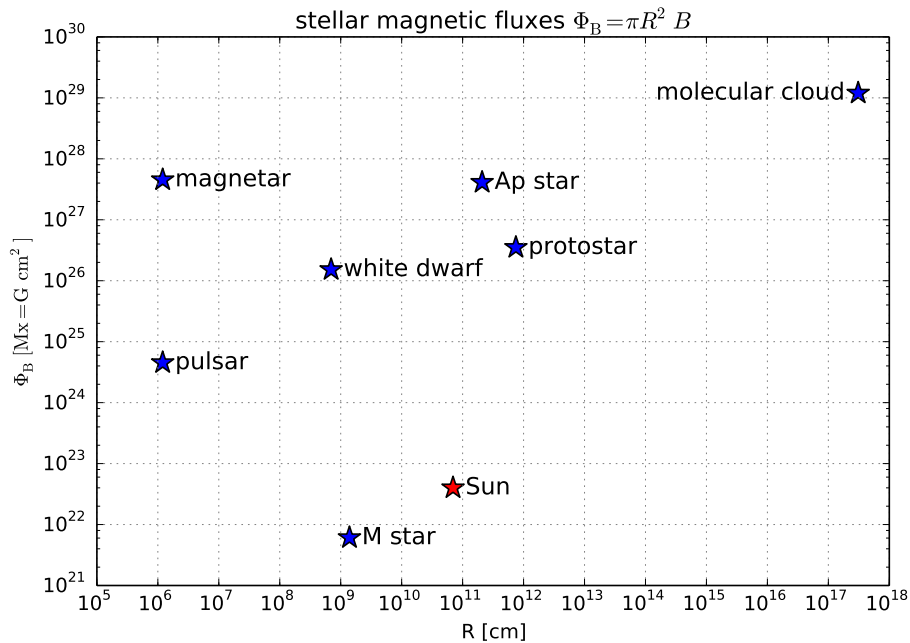
Figure 2: Solution to Problem 5. Magnetic flux Φ_{B} across a stellar object as function of its radius R.

- The effect of P is not strong, e.g., Venus and Mars have comparably failed dynamos with $\Lambda < 10^{-10}$.

- The cores of Earth, Ganymede and Jupiter have similar $\Lambda \sim 3 \times 10^{-4}$. For Earth, the total core field (inc. toroidal) $B_{\mathrm{tot}} \simeq 25$ G implies $\Lambda \simeq 3$. Dipole fields are not enough to demonstrate the hypothesis that the Lorentz forces may balance the Coriolis forces ($\Lambda \sim 1$).

- The dynamo of Mercury is rather weak with $\Lambda \sim 3 \times 10^{-8}$, its large core makes significant difference from Ganymede.

Problem 5 (stellar magnetic fluxes).   Estimate order-of-magnitude magnetic fluxes Φ_{B} across:

- a molecular cloud ($B \sim 0.4$ mG, $R \sim 0.1$ pc);

- a low-mass (T Tau) protostar ($B \sim 200$ G, $R \sim 0.05$ AU);

- a low mass ($0.1 M_\odot$) M star ($B \sim 1$ kG);

- the Sun ($B \sim 2.5$ G);

- a high-mass ($2.5 M_\odot$) Ap star ($B \sim 30$ kG);

- a strongly magnetized white dwarf ($B \sim 10^8$ G);

- a pulsar ($B \sim 10^{12}$ G);

- a magnetar ($B \sim 10^{15}$ G).

Stellar radii R can be read from the Hertzsprung-Russell diagram. For neutron stars adopt $R \simeq 12$ km. Create a log-log diagram of magnetic flux Φ_{B} vs. radius R. What basic conclusions can be made?

Solution to Problem 5. The diagram of magnetic flux $\Phi_{\mathrm{B}} = \pi R^2 B$ vs. radius R is presented in Figure 2. From the HR diagram, we read the following stellar radii:

- $\sim 0.02 R_\odot$ for a $0.1 M_\odot$ main-sequence star;

- $\sim 3 R_\odot$ for a $2.5 M_\odot$ main-sequence star;

- $\sim 0.01 R_\odot$ for a white dwarf.

A few basic conclusions can be drawn from this diagram:

- In the scenario of forming the Sun from a molecular cloud of given parameters through the T Tau protostellar stage, strong reduction of Φ_{B} is necessary during the formation of both the protostar and the main sequence star.

- The magnetic flux of the Sun is insufficient to form a highly magnetized white dwarf (without a dynamo mechanism).

- The magnetic flux of an Ap star is comparable to that of a magnetar, which suggests that the fossil field hypothesis for the origin of magnetar fields is plausible (although it would require a very high efficiency of preserving the stellar Φ_{B}).

References

Abdollahi, S., Acero, F., Ackermann, M., et al. 2020, ApJS, 247, 33. doi:10.3847/1538-4365/ab6bcb

Ackermann, M., Anantua, R., Asano, K., et al. 2016, ApJ, 824, L20. doi:10.3847/2041-8205/824/2/L20

Aharonian, F., Akhperjanian, A. G., Bazer-Bachi, A. R., et al. 2006, Science, 314, 1424. doi:10.1126/science.1134408

Aharonian, F., Akhperjanian, A. G., Bazer-Bachi, A. R., et al. 2007, ApJ, 664, L71. doi:10.1086/520635

Algaba, J. C., Asada, K., & Nakamura, M. 2016, ApJ, 823, 86. doi:10.3847/0004-637X/823/2/86

Anderson, B. J., Johnson, C. L., Korth, H., et al. 2011, Science, 333, 1859. doi:10.1126/science.1211001

Angelakis, E., Hovatta, T., Blinov, D., et al. 2016, MNRAS, 463, 3365. doi:10.1093/mnras/stw2217

Armitage, P. J. 2011, ARA&A, 49, 195. doi:10.1146/annurev-astro-081710-102521

Baade, W. 1956, ApJ, 123, 550. doi:10.1086/146194

Babcock, H. W. 1947, ApJ, 105, 105. doi:10.1086/144887

Babcock, H. W. 1960, ApJ, 132, 521. doi:10.1086/146960

Baker, D. N., Li, X., Pulkkinen, A., et al. 2013, Space Weather, 11, 585. doi:10.1002/swe.20097

Bale, S. D., Badman, S. T., Bonnell, J. W., et al. 2019, Nature, 576, 237. doi:10.1038/s41586-019-1818-7

Basu, A., Wadadekar, Y., Beelen, A., et al. 2015, ApJ, 803, 51. doi:10.1088/0004-637X/803/2/51

Basu, A., Mao, S. A., Kepley, A. A., et al. 2017, MNRAS, 464, 1003. doi:10.1093/mnras/stw2369

Beck, R. 2015, A&ARv, 24, 4. doi:10.1007/s00159-015-0084-4

Berger, M. A. & Ruzmaikin, A. 2000, JGR, 105, 10481. doi:10.1029/1999JA900392

Biermann, L. 1951, ZA, 29, 274

Biretta, J. A., Sparks, W. B., & Macchetto, F. 1999, ApJ, 520, 621. doi:10.1086/307499

Blandford, R. & Eichler, D. 1987, Physics Reports, 154, 1. doi:10.1016/0370-1573(87)90134-7

Boro Saikia, S., Marvin, C. J., Jeffers, S. V., et al. 2018, A&A, 616, A108. doi:10.1051/0004-6361/201629518

Buffett, B. A. 2010, Nature, 468, 952. doi:10.1038/nature09643

Butsky, I., Zrake, J., Kim, J.-H., et al. 2017, ApJ, 843, 113. doi:10.3847/1538-4357/aa799f

Capetti, A., Brienza, M., Balmaverde, B., et al. 2022, arXiv:2202.08593

Carrington, R. C. 1859, MNRAS, 20, 13. doi:10.1093/mnras/20.1.13

Charbonneau, P. 2014, ARA&A, 52, 251. doi:10.1146/annurev-astro-081913-040012

Crutcher, R. M. 1999, ApJ, 520, 706. doi:10.1086/307483

Cooray, A. 2016, Royal Society Open Science, 3, 150555. doi:10.1098/rsos.150555

Donati, J.-F. & Landstreet, J. D. 2009, ARA&A, 47, 333. doi:10.1146/annurev-astro-082708-101833

Event Horizon Telescope Collaboration: Akiyama, K., Alberdi, A., et al. 2019.I, ApJ, 875, L1. doi:10.3847/2041-8213/ab0ec7

Event Horizon Telescope Collaboration: Akiyama, K., Alberdi, A., et al. 2019.V, ApJ, 875, L5. doi:10.3847/2041-8213/ab0f43

Event Horizon Telescope Collaboration: Akiyama, K., Algaba, J. C., et al. 2021.VII, ApJ, 910, L12. doi:10.3847/2041-8213/abe71d

Fanaroff, B. L. & Riley, J. M. 1974, MNRAS, 167, 31P. doi:10.1093/mnras/167.1.31P

Feinstein, A. D., Seligman, D. Z., Günther, M. N., et al. 2022, ApJ, 925, L9. doi:10.3847/2041-8213/ac4b5e

Fender, R. P., Garrington, S. T., McKay, D. J., et al. 1999, MNRAS, 304, 865. doi:10.1046/j.1365-8711.1999.02364.x

Fermi, E. 1949, Physical Review, 75, 1169. doi:10.1103/PhysRev.75.1169

Fletcher, A., Beck, R., Shukurov, A., et al. 2011, MNRAS, 412, 2396. doi:10.1111/j.1365-2966.2010.18065.x

Fossati, G., Maraschi, L., Celotti, A., et al. 1998, MNRAS, 299, 433. doi:10.1046/j.1365-8711.1998.01828.x

Fromm, C. M., Ros, E., Perucho, M., et al. 2013, A&A, 557, A105. doi:10.1051/0004-6361/201321784

Güdel, M. & Benz, A. O. 1993, ApJ, 405, L63. doi:10.1086/186766

Hale, G. E. 1908, ApJ, 28, 315. doi:10.1086/141602

Hale, G. E., Ellerman, F., Nicholson, S. B., et al. 1919, ApJ, 49, 153. doi:10.1086/142452

Halley, E. 1683, Philosophical Transactions of the Royal Society of London Series I, 13, 208

Hada, K., Kino, M., Doi, A., et al. 2016, ApJ, 817, 131. doi:10.3847/0004-637X/817/2/131

Harris, D. E., Cheung, C. C., Stawarz, Ł., et al. 2009, ApJ, 699, 305. doi:10.1088/0004-637X/699/1/305

Hester, J. J., Mori, K., Burrows, D., et al. 2002, ApJ, 577, L49. doi:10.1086/344132

Hillas, A. M. 1984, ARA&A, 22, 425. doi:10.1146/annurev.aa.22.090184.002233

Howe, R. 2009, Living Reviews in Solar Physics, 6, 1. doi:10.12942/lrsp-2009-1

Hutton, C. 1778, Philosophical Transactions of the Royal Society of London Series I, 68, 689

Jansson, R. & Farrar, G. R. 2012, ApJ, 757, 14. doi:10.1088/0004-637X/757/1/14

Jiang, C., Feng, X., Liu, R., et al. 2021, Nature Astronomy, 5, 1126. doi:10.1038/s41550-021-01414-z

Junor, W., Biretta, J. A., & Livio, M. 1999, Nature, 401, 891. doi:10.1038/44780

Kim, J.-Y., Krichbaum, T. P., Lu, R.-S., et al. 2018, A&A, 616, A188. doi:10.1051/0004-6361/201832921

Kitchatinov, L. L. & Rüdiger, G. 2004, A&A, 424, 565. doi:10.1051/0004-6361:20040431

Krause, M., Irwin, J., Schmidt, P., et al. 2020, A&A, 639, A112. doi:10.1051/0004-6361/202037780

Lister, M. L., Homan, D. C., Hovatta, T., et al. 2019, ApJ, 874, 43. doi:10.3847/1538-4357/ab08ee

Lopez-Rodriguez, E., Guerra, J. A., Asgari-Targhi, M., et al. 2021, ApJ, 914, 24. doi:10.3847/1538-4357/abf934

Madrid, J. P. 2009, AJ, 137, 3864. doi:10.1088/0004-6256/137/4/3864

Masters, A., Stawarz, L., Fujimoto, M., et al. 2013, Nature Physics, 9, 164. doi:10.1038/nphys2541

Mirabel, I. F. & Rodríguez, L. F. 1994, Nature, 371, 46. doi:10.1038/371046a0

Mirabel, I. F. & Rodríguez, L. F. 1998, Nature, 392, 673. doi:10.1038/33603

Mouschovias, T. C. & Spitzer, L. 1976, ApJ, 210, 326. doi:10.1086/154835

Nalewajko, K., Begelman, M. C., & Sikora, M. 2014, ApJ, 789, 161. doi:10.1088/0004-637X/789/2/161

Nalewajko, K., Sikora, M., & Różańska, A. 2020, A&A, 634, A38. doi:10.1051/0004-6361/201936586

Nalewajko, K. 2021, arXiv:2111.07735

Oppermann, N., Junklewitz, H., Robbers, G., et al. 2012, A&A, 542, A93. doi:10.1051/0004-6361/201118526

Owen, F. N., Eilek, J. A., & Kassim, N. E. 2000, ApJ, 543, 611. doi:10.1086/317151

Parker, E. N. 1958, ApJ, 128, 664. doi:10.1086/146579

Pasetto, A., Carrasco-González, C., Gómez, J. L., et al. 2021, ApJ, 923, L5. doi:10.3847/2041-8213/ac3a88

Pesce-Rollins, M., Omodei, N., Petrosian, V., et al. 2015, ApJ, 805, L15. doi:10.1088/2041-8205/805/2/L15

Planck Collaboration, Adam, R., Ade, P. A. R., et al. 2016, A&A, 594, A1. doi:10.1051/0004-6361/201527101

Punsly, B. & Chen, S. 2021, ApJ, 921, L38. doi:10.3847/2041-8213/ac33b6

Purkhart, S. & Veronig, A. M. 2022, arXiv:2203.11625

Roberts, P. H. & King, E. M. 2013, Reports on Progress in Physics, 76, 096801. doi:10.1088/0034-4885/76/9/096801

Roettenbacher, R. M., Monnier, J. D., Korhonen, H., et al. 2016, Nature, 533, 217. doi:10.1038/nature17444

Rüdiger, G. & Hollerbach, R. 2004, The Magnetic Universe: Geophysical and Astrophysical Dynamo Theory, pp. 343. ISBN 3-527-40409-0. Wiley-VCH , August 2004., 343

Saar, S. H. & Brandenburg, A. 1999, ApJ, 524, 295. doi:10.1086/307794

Schmidt, M. 1963, Nature, 197, 1040. doi:10.1038/1971040a0

Sikora, M., Begelman, M. C., & Rees, M. J. 1994, ApJ, 421, 153. doi:10.1086/173633

Sikora, M., Stawarz, Ł., Moderski, R., et al. 2009, ApJ, 704, 38. doi:10.1088/0004-637X/704/1/38

Spitkovsky, A. 2008, ApJ, 682, L5. doi:10.1086/590248

Stähler, S. C., Khan, A., Banerdt, W. B., et al. 2021, Science, 373, 443. doi:10.1126/science.abi7730

Stevenson, D. J. 1983, Reports on Progress in Physics, 46, 555. doi:10.1088/0034-4885/46/5/001

Strassmeier, K. G. 1999, A&A, 347, 225

Tavecchio, F. & Ghisellini, G. 2016, MNRAS, 456, 2374. doi:10.1093/mnras/stv2790

Uchiyama, Y., Urry, C. M., Cheung, C. C., et al. 2006, ApJ, 648, 910. doi:10.1086/505964

Uchiyama, Y., Aharonian, F. A., Tanaka, T., et al. 2007, Nature, 449, 576. doi:10.1038/nature06210

Urry, C. M. & Padovani, P. 1995, PASP, 107, 803. doi:10.1086/133630

van Weeren, R. J., Röttgering, H. J. A., Brüggen, M., et al. 2010, Science, 330, 347. doi:10.1126/science.1194293

Walker, R. C., Hardee, P. E., Davies, F. B., et al. 2018, ApJ, 855, 128. doi:10.3847/1538-4357/aaafcc

Zamaninasab, M., Clausen-Brown, E., Savolainen, T., et al. 2014, Nature, 510, 126. doi:10.1038/nature13399